

Unveiling the Velocity-Space Signature of Ion Cyclotron Damping Using Liouville Mapping

Rui Huang¹ and Gregory G. Howes¹

Department of Physics and Astronomy, University of Iowa, Iowa City, IA 52242, USA.

(*Electronic mail: rui-huang@uiowa.edu)

(Dated: 30 July 2025)

Ion cyclotron damping is a key mechanism for the dissipation of electromagnetic wave energy in weakly collisional plasmas. This study presents a combined approach using Liouville mapping and the field-particle correlation technique to investigate qualitatively and quantitatively the velocity-space signature of ion cyclotron damping. Liouville mapping offers a computationally efficient way to predict perturbations to the particle velocity distribution function using single-particle trajectories in prescribed electromagnetic fields. One may apply the field-particle correlation technique to these perturbed velocity distributions to reveal the unique velocity-space signatures of the secular energy transfer rate associated with specific wave-particle interactions. We validate this method by reproducing known Landau damping signatures for kinetic Alfvén waves, and then we apply this method to ion cyclotron waves where ion cyclotron damping dominates. The resulting velocity-space signature reveals distinct energization features of ion cyclotron damping : (i) a quadrupolar pattern in the perpendicular (v_x, v_y) plane; and (ii) a localized energization near the $n = 1$ resonant velocity in gyrotropic $(v_{\parallel}, v_{\perp})$ velocity-space. The quantitative patterns remain unchanged as the ion plasma beta β_i is varied, ultimately showing minimal v_{\perp} dependence on β_i of the velocity-space signature at the $n = 1$ resonant velocity. This work provides the first systematic study of how the ion cyclotron damping velocity-space signature varies with β_i , offering a practical foundation to identify ion cyclotron damping using kinetic simulation data or spacecraft data.

I. INTRODUCTION

The dissipation of turbulence and the resulting heating of the plasma species play a fundamental role in the evolution of astrophysical and heliospheric plasmas. Identifying the physical mechanisms underlying the observed steepening of the turbulent energy power spectrum at small scales¹ remains an open question in heliophysics. The physics of this turbulent dissipation involves a number of potential processes²: (1) resonant wave-particle interactions such as Landau damping, transit-time damping, and cyclotron damping; (2) non-resonant wave-particle interactions including stochastic heating, magnetic pumping, and viscous-like damping from kinetic temperature anisotropy instabilities; and (3) dissipation within coherent structures, such as collisionless magnetic reconnection occurring in turbulence-generated current sheets.

Identifying the physical mechanisms in turbulent plasmas is critical for linking the observed spectral features to the underlying physics. Such insight has the potential to enhance our ability to interpret observations of turbulence in space plasmas and is essential to the development of predictive models of the turbulent plasma heating². One approach is to compute the energy transfer rate based on the fluid description using measurements of the field and plasma fluctuations and compare that rate to theoretical predictions for specific processes. However, this method often proves inconclusive when multiple turbulent damping mechanisms contribute to the dissipation, especially since those mechanisms generally scale differently with the fundamental parameters of the plasma and turbulence. Furthermore, this fluid approach underutilizes the rich phase-space information available in the measured velocity distributions of the plasma species.

A more effective approach based on kinetic theory is the field-particle correlation (FPC) technique. First defined by

Klein & Howes (2016)³, the FPC has the mathematical form of a modified statistical correlation between the electric field measurements and particle distribution function collected at one spatial point over an observed time interval⁴. Physically, the FPC quantifies the velocity-space distribution of the secular energy transfer rate from the electromagnetic field to the particles as a function of the three-dimensional (3V) space of particle velocity. These velocity-space distributions are found to display characteristic patterns associated with specific dissipation mechanisms, enabling the identification of specific mechanisms, even if cases where multiple mechanisms are acting coincidentally^{5,6}. More importantly, these patterns associated with well-known wave-particle interactions—such as Landau damping or transit-time damping—persist even in turbulent data, enabling a clear identification of the channels of turbulent energy dissipation^{5–14}.

To determine whether a specific mechanism contributes to the damping of turbulence in a given simulation or observation, one must first discover that mechanism's unique velocity-space signature. This is typically achieved through well-controlled simulations where that single mechanism dominates by carefully selecting the simulation parameters. The FPC computed from such simulation data reveals a characteristic pattern of the particle energization in velocity space that is then used to identify the mechanism, known as the *velocity-space signature*. Once these velocity-space signatures are established for each proposed damping mechanism, we can analyze the given turbulent datasets. By computing the FPC from the turbulent data and comparing the resulting velocity-space signature with the known signatures, we can determine which physical mechanisms are active. A close match between the turbulent FPC and a known signature provides strong evidence that the corresponding mechanism contributes to energy dissipation in that system.

For instance, the FPC technique has been successfully ap-

plied to kinetic numerical simulations to discover the velocity-space signatures of Landau damping^{3,4,13}, transit-time damping¹⁴, cyclotron damping⁵, magnetic pumping¹⁵, magnetic reconnection¹⁶, and collisionless shocks^{17–20}. Guided by these revealed signatures, the FPC technique has been utilized to identify these physical mechanisms in real-world data, from lab experiments²¹ to spacecraft observations^{6,11,22}.

From a methodological perspective, the prerequisite for applying the FPC technique to identify physical mechanisms from turbulent datasets is the discovery of unique velocity-space signatures corresponding to each mechanism. This initial “signature discovery” step is often limited by the cost and complexity of generating well-controlled data, particularly the velocity distribution function data. For example, Klein *et al.* (2020)⁵ discovers the velocity-space signature of ion cyclotron damping using hybrid Vlasov-Maxwell simulations of Alfvénic-ion turbulence, but these simulations are computationally expensive and offer limited flexibility to explore parameter dependencies.

A promising way to address this constraint is the Liouville mapping technique, as detailed in Schwartz *et al.* (1998)²³. Based on Liouville’s theorem, which states that the phase-space distribution function remains constant along a particle’s trajectory, this method reconstructs the distribution function by tracking single-particle orbits in known electromagnetic fields, bypassing the direct solving of the Vlasov-Maxwell equation system. Previous work²¹ applies this method to calculate FPC for one-dimensional Landau damping in comparison with laboratory measurements. To date, however, the Liouville mapping method remains underexplored as a general approach to predict the velocity-space signatures of different turbulent damping mechanisms, particularly in three-dimensional contexts.

From a physics perspective, resonant wave-particle interactions are widely recognized as fundamental processes for turbulent energy transfer^{6,11,12}, yet important gaps remain. For example, the 3V velocity-space signature of ion cyclotron damping and its dependence on the ion plasma beta β_i (the ratio of the ion thermal to the magnetic pressure) has not been systematically explored.

Motivated by these considerations, this study employs the Liouville mapping technique to generate well-controlled data for exploring the detailed velocity-space signatures of two resonant wave-particle interactions: Landau damping and cyclotron damping. The Landau damping case, having been thoroughly studied in previous work, serves primarily to validate the method, while the cyclotron damping case is the focus of new physics uncovered by our method. This paper is structured as follows. Section II provides a detailed overview of diagnosing the secular energy transfer from the electromagnetic field to the particles in resonance using FPC. Section III describes how the Liouville mapping technique is incorporated into the FPC computation. Section IV presents results for ion Landau damping as the method validation. Section V displays the key findings of this work: the detailed velocity-space signatures of ion cyclotron damping. The properties of ion cyclotron damping are outlined in Section V A. The velocity-space signature presented in the (v_x, v_y) and $(v_{\parallel}, v_{\perp})$ planes

is shown in Section V B, with corresponding interpretations given in Section V C and Section V D. Finally, Section V E presents the first analysis of the dependence of ion cyclotron damping velocity-space signature on β_i .

The definitions of important physical quantities used in this paper can be found in Table I.

II. THE PHYSICS OF RESONANT WAVE-PARTICLE INTERACTIONS

The primary objective of this study is to characterize resonant wave-particle interactions using single-point measurement data. These interactions between the charged particles and plasma waves satisfy the resonance condition

$$\omega - k_{\parallel} v_{\text{res}, n} = n\Omega_s. \quad (1)$$

The left-hand side of Eq. (1) represents the Doppler-shifted wave frequency in the reference frame moving with the particle’s parallel velocity; the resonance occurs when that Doppler shifted frequency is equal to a harmonic of the cyclotron frequency Ω_s of particle species s , where the integer $n = 0, \pm 1, \pm 2, \dots$ arises from a Bessel expansion for the plane wave²⁴. Here ω is the wave frequency and \mathbf{k} is wavevector, where k_{\parallel} is its component along the equilibrium magnetic field direction, $\mathbf{B}_0 = B_0 \hat{\mathbf{z}}$. Note that the $n = 0$ resonance corresponds to Landau resonance, the $|n| > 0$ resonance correspond to the fundamental and harmonics of cyclotron resonance. Within the scope of this study, which focuses on parallel-propagating wave modes, only $n = 0, \pm 1$ resonances are expected²⁵.

To analyze these interactions, we employ the field-particle correlation technique, which is rooted in the Vlasov equation describing the evolution of the distribution function $f_s(\mathbf{r}, \mathbf{v}, t)$ for particles of species s in a collisionless plasma:

$$\frac{\partial f_s}{\partial t} + \mathbf{v} \cdot \frac{\partial f_s}{\partial \mathbf{r}} + \frac{q_s}{m_s} \left(\mathbf{E} + \frac{\mathbf{v} \times \mathbf{B}}{c} \right) \cdot \frac{\partial f_s}{\partial \mathbf{v}} = 0 \quad (2)$$

The interaction between the electromagnetic fields and the particle distribution function is encoded in the third term on the left-hand side of the equation. Multiplying by $(1/2)m_s v^2$ and defining the phase-space energy density as $w_s(\mathbf{r}, \mathbf{v}, t) \equiv (1/2)m_s v^2 f_s$, we obtain its evolution:

$$\frac{\partial w_s}{\partial t} = -\mathbf{v} \cdot \frac{\partial w_s}{\partial \mathbf{r}} - \frac{1}{2} q_s v^2 \mathbf{E} \cdot \frac{\partial f_s}{\partial \mathbf{v}} - \frac{1}{2} q_s v^2 \frac{\mathbf{v} \times \mathbf{B}}{c} \cdot \frac{\partial f_s}{\partial \mathbf{v}} \quad (3)$$

Within a chosen spatial volume, the total microscopic kinetic energy contained in the particles, $\mathcal{W}_s = \int w_s d\mathbf{v} d\mathbf{r}$, changes only due to the electric field in the second term. Integrating the electric field term over velocity space yields the rate of change of energy density of species s due to work done by the electric field, $\mathbf{J}_s \cdot \mathbf{E}$, where \mathbf{J}_s denotes the current density from the motion of particles of species s . The advection term (first term) vanishes under either infinite or periodic spatial boundary conditions, and the magnetic term (third term) redistributes particles in velocity space but does not alter the total energy⁴.

TABLE I. Definitions of Important Physical Quantities Used in this Paper

Quantity	Definition	Quantity	Definition
s	Particle species	$v_{ts} = \sqrt{2T_{0s}/m_s}$	Particle thermal speed
m_s	Mass	c	Speed of light
q_s	Charge	$\Omega_s = q_s B_0 / (m_s c)$	Species cyclotron frequency
\mathbf{v}	Particle velocity	$\rho_s = v_{ts} / \Omega_s$	Species Larmor radius
B_0	Equilibrium magnetic field	$v_A = B_0 / \sqrt{4\pi m_i n_{0i}}$	Alfvén speed
n_{0s}	Species number density	$\beta_i = 8\pi n_{0i} T_{0i} / B_0^2 = v_{ti}^2 / v_A^2$	Ion plasma beta
T_{0s}	Species temperature (units: eV)	$\mathbf{k} = k_\perp \hat{x} + k_\parallel \hat{z}$	Wave vector
$f_s(\mathbf{r}, \mathbf{v}, t)$	Distribution function	ω, γ	Wave frequency and growth rate
$\mathbf{E}(\mathbf{r}, t)$	Electric field	$w_s(\mathbf{r}, \mathbf{v}, t) \equiv (1/2)m_s v^2 f_s$	Phase-space energy density
$\mathbf{B}(\mathbf{r}, t)$	Magnetic field	$W_s(\mathbf{r}, t) \equiv \int w_s d\mathbf{v}$	Energy density
$\mathbf{J}_s(\mathbf{r}, t)$	Species current density	$\mathcal{W}_s(t) \equiv \int W_s d\mathbf{r}$	Energy

Based on the electric field term in Eq. (3), the field-particle correlation (FPC) technique is developed. The correlations for species s , $C_{E_x,s}$, $C_{E_y,s}$, $C_{E_\parallel,s}$ and $C_{E_\perp,s}$, computed at a fixed spatial location \mathbf{r}_0 and centered at time t_0 , are defined as

$$C_{E_x,s}(\mathbf{r}_0, \mathbf{v}, t_0; \tau) \equiv \frac{1}{\tau} \int_{t_0-\tau/2}^{t_0+\tau/2} \left[-q_s \frac{v_x^2}{2} \frac{\partial f_s(\mathbf{r}_0, \mathbf{v}, t)}{\partial v_x} E_x(\mathbf{r}_0, t) \right] dt, \quad (4)$$

$$C_{E_y,s}(\mathbf{r}_0, \mathbf{v}, t_0; \tau) \equiv \frac{1}{\tau} \int_{t_0-\tau/2}^{t_0+\tau/2} \left[-q_s \frac{v_y^2}{2} \frac{\partial f_s(\mathbf{r}_0, \mathbf{v}, t)}{\partial v_y} E_y(\mathbf{r}_0, t) \right] dt, \quad (5)$$

$$C_{E_\parallel,s}(\mathbf{r}_0, \mathbf{v}, t_0; \tau) = C_{E_z,s}(\mathbf{r}_0, \mathbf{v}, t_0; \tau) \equiv \frac{1}{\tau} \int_{t_0-\tau/2}^{t_0+\tau/2} \left[-q_s \frac{v_z^2}{2} \frac{\partial f_s(\mathbf{r}_0, \mathbf{v}, t)}{\partial v_z} E_z(\mathbf{r}_0, t) \right] dt, \quad (6)$$

$$C_{E_\perp,s}(\mathbf{r}_0, \mathbf{v}, t_0; \tau) \equiv C_{E_x,s}(\mathbf{r}_0, \mathbf{v}, t_0; \tau) + C_{E_y,s}(\mathbf{r}_0, \mathbf{v}, t_0; \tau) \quad (7)$$

where these correlations are time-averaged over an appropriately chosen correlation interval τ . Note that the v^2 in the electric field term in Eq. (3) is replaced in these definitions by v_j^2 , where the field component is indicated the index j —this replacement yields no change in the velocity-integrated rate of change of energy density⁴.

Each of the correlations in Eqs. (4)–(7) quantifies how the different components of the electric field (E_x , E_y , E_\parallel or E_\perp) contribute to the time-averaged rate of change of the phase-space energy density $w_s(\mathbf{r}_0, \mathbf{v}, t_0)$. With a suitably chosen correlation interval τ , the field-particle correlation isolates the secular energy transfer between the electric field and the particles by the cancellation of any oscillatory energy transfer over its characteristic oscillation period⁴. Effectively, the FPC captures the long-timescale rate of change of the phase-space energy density, given by $\frac{\partial}{\partial t_0} \left(\frac{1}{\tau} \int_{t_0-\tau/2}^{t_0+\tau/2} w_s dt \right)^{26}$. When integrated over 3-dimensional (3V) velocity space, the FPC yields a quantitative determination of the rate of change of spatial energy density, $W_s(\mathbf{r}_0, t) = \int w_s(\mathbf{r}_0, \mathbf{v}, t) d\mathbf{v}$.

At a particular spatial point \mathbf{r}_0 and time t_0 , the field-particle correlation $C_{E_j,s}(v_x, v_y, v_z)$ due to electric field component E_j produces a pattern representing the rate of energy transfer to the particles throughout 3V velocity space, known as the *velocity-space signature* of the particle energization. The FPCs in 3V velocity space are usually expressed in either cylindrical ($v_\parallel, \theta, v_\perp$) or Cartesian (v_x, v_y, v_z) coordinates. For simplicity, we use the notation $C_{E_j,s}(v_\parallel, \theta, v_\perp)$ or $C_{E_j,s}(v_x, v_y, v_z)$ with $j = x, y, \parallel, \perp$, and explicitly denote \mathbf{r}_0, t_0 , and τ only when necessary.

The velocity-space signatures generated by the FPC technique are most easily visualized by reducing the 3V information to a 2V plane that emphasizes the features of the particular kinetic energization mechanism. For example, previous studies show that plotting $C_{E_\parallel,s}$ on the gyrotropic plane (v_\parallel, v_\perp) captures the features of Landau damping, so we integrate the full cylindrical 3V correlation over gyroangle θ , denoting the 2V correlation by $C_{E_\parallel,s}(v_\parallel, v_\perp)$. Similarly, for ion cyclotron damping, integrating over the parallel v_z dimension yields helpful characterizations of the energization by $C_{E_x,s}$, $C_{E_y,s}$, and $C_{E_\perp,s}$ on the 2V (v_x, v_y) plane. Generally, different kinetic mechanisms of particle energization yield unique velocity-space signatures that can be used to identify the mechanism from single-point, time-series measurements of the 3V velocity distributions $f_s(\mathbf{r}_0, \mathbf{v}, t)$ and the electric field $\mathbf{E}(\mathbf{r}_0, t)$. Below, we describe how we use Liouville mapping to obtain these quantities in computationally efficient way.

III. LIOUVILLE MAPPING PROCEDURE

A. Overview

In plasma physics, the Liouville theorem in Hamiltonian mechanics takes the form of the Vlasov equation, Eq. (2), where the left hand side of represents the Lagrangian derivative along a particle trajectory in phase space, while the right hand side is zero. This implies that the distribution function remains constant along a particle's trajectory in 3D-3V phase space. Specifically,

$$f_s(\mathbf{r}(t_1), \mathbf{v}(t_1), t_1) = f_s(\mathbf{r}(t_2), \mathbf{v}(t_2), t_2), \quad (8)$$

where t_1 and t_2 are two different time samples, and the position $\mathbf{r}(t)$ together with the velocity $\mathbf{v}(t)$ gives the particle's trajectory in phase space. To track these trajectories, we numerically integrate the following single particle motion equations

$$\frac{d\mathbf{r}}{dt} = \mathbf{v}, \quad (9)$$

$$\frac{d\mathbf{v}}{dt} = \frac{q_s}{m_s} \left(\mathbf{E} + \frac{\mathbf{v}}{c} \times \mathbf{B} \right). \quad (10)$$

This allows us to map the distribution function between different times if the spatial and temporal variations of the electromagnetic fields are known²³. While conceptually straightforward, its practical implementation for FPC calculation involves several technical steps, as outlined below.

B. Constructing electromagnetic fields

The electromagnetic fields for Liouville mapping are constructed by inverse Fourier transforming numerically obtained eigenfunctions. These eigenfunctions are computed as functions of the wavevector $\mathbf{k} = k_\perp \hat{x} + k_\parallel \hat{z}$ using the FORTRAN 90 code PLUME^{27,28}, which solves the dispersion relation of the linearized Vlasov-Maxwell equations in Fourier space, describing a collisionless, hot, uniformly magnetized ion-electron plasma, as formulated in Chapter 10, Eqs. (66)–(73) of Stix (1992)²⁴. PLUME requires specification of five key dimensionless input parameters: the normalized parallel and the perpendicular components of the wavevector, $k_\parallel \rho_i$ and $k_\perp \rho_i$; ion plasma beta β_i ; ion-to-electron temperature ratio T_i/T_e ; and normalized ion thermal velocity v_{ti}/c . We specify protons as the ion species by choosing the ion-to-electron mass ratio $m_i/m_e = 1836$. Outputs from PLUME include the wave frequency ω and growth or damping rate γ (positive for growth, negative for damping) normalized to the ion cyclotron frequency Ω_i , as well as the complex Fourier coefficients of the vector electric and magnetic field eigenfunctions.

To present how we construct the electromagnetic fields in space and time, we let \mathbf{F} denote either the electric field \mathbf{E} or magnetic field \mathbf{B} , and express each total field as a sum of an equilibrium component and a perturbation

$$\mathbf{F}(\mathbf{r}, t) = \mathbf{F}_0 + W(t; t_{\text{init}}, t') \sum_{l=1}^n \delta \mathbf{F}_l(\mathbf{r}, t). \quad (11)$$

Here the first term, \mathbf{F}_0 , is the equilibrium field, with $\mathbf{E}_0 = 0$ and $\mathbf{B}_0 = B_0 \hat{z}$. The second term represents the total perturbed field due to a linear superposition of n linear wave modes, where $\delta \mathbf{F}_l(\mathbf{r}, t)$ is the perturbed field contributed by the l -th wave mode, given by

$$\delta \mathbf{F}_l(\mathbf{r}, t) = \frac{\varepsilon_l}{2} \left\{ \delta \hat{\mathbf{F}}(\mathbf{k}_l) \exp[i(\mathbf{k}_l \cdot \mathbf{r} - \omega(\mathbf{k}_l)t + \alpha_l)] + \delta \hat{\mathbf{F}}^*(\mathbf{k}_l) \exp[-i(\mathbf{k}_l \cdot \mathbf{r} - \omega(\mathbf{k}_l)t + \alpha_l)] \right\}, \quad (12)$$

where \mathbf{k}_l , $\omega(\mathbf{k}_l)$ and $\delta \hat{\mathbf{F}}(\mathbf{k}_l)$ are the wavevector, real wave frequency, and complex field Fourier coefficients for the l -th mode, respectively. The hat symbol $\hat{}$ indicates quantities in Fourier space, the notational dependence (\mathbf{k}_l) emphasizes that these quantities are functions of the wavevector, and the asterisk $*$ denotes the complex conjugate. An arbitrary real phase $0 \leq \alpha_l < 2\pi$ is allowed for each wave mode l to adjust the relative phase among multiple modes. Note that we neglect the growth or damping rate $\gamma(\mathbf{k}_l)$ for all modes so that the each wave mode retains a constant peak amplitude in time. The amplitude for each wave mode is directly controlled by a dimensionless amplitude factor ε_l , defined by

$$\varepsilon_l = \frac{c \delta \hat{E}_x(\mathbf{k}_l)}{v_{ti} B_0}, \quad (13)$$

where $v_{ti} = \sqrt{2T_{0i}/m_i}$ is the ion thermal speed. In the magnetohydrodynamic (MHD) limit, this amplitude factor ε_l is related to the magnitude of the magnetic field perturbation of an Alfvén wave normalized to the equilibrium field by $\delta \hat{B}_y/B_0 = \pm c \sqrt{\beta_i} \delta \hat{E}_x/(v_{ti} B_0)$.

The time-dependent window function $W(t; t_{\text{init}}, t')$ smoothly ramps up the perturbation over duration t'

$$W(t; t_{\text{init}}, t') = \begin{cases} \frac{1}{2} \left[1 - \cos\left(\frac{\pi t}{t'}\right) \right], & t_{\text{init}} \leq t \leq t_{\text{init}} + t' \\ 1, & t > t_{\text{init}} + t', \end{cases} \quad (14)$$

Here, t_{init} marks the start of system evolution. This gradual ramp-up of the wave amplitude eliminates artifacts in the perturbed distribution function associated with the Liouville mapping. By mapping back to a time t_{init} at which the wave amplitude is zero, one may map to a chosen analytical form for the equilibrium velocity distribution function *in the absence of waves*, meaning that the initial distribution is uniform in space. Since particles starting at the same position but with different velocities will generally be mapped to different positions in space over the same time interval, this would lead to undesired perturbations in the velocity distribution function unless the wave amplitude is zero at t_{init} .

In this study, we consider two types of field configurations: (i) a single propagating wave mode with wavevector \mathbf{k} , and (ii) a pair of counter-propagating waves with wavevectors $\mathbf{k} = (k_x, k_y, \pm k_z)$, forming a standing wave along the z -direction. In both cases, the perturbed field is periodic with $T = 2\pi/\omega$. We set $t' = T$ in the window function, Eq. (14), so that the field amplitude ramps up over its first wave period.

This procedure enables the analytical specification of the full spatial and temporal variation of the electric and magnetic fields, $\mathbf{E}(\mathbf{r}, t)$ and $\mathbf{B}(\mathbf{r}, t)$, where the form of Eq. (11) effectively leads to a linear superposition of plane waves that pervade all space. This specification also yields the first key quantity needed for computing FPC, the electric field $\mathbf{E}(\mathbf{r}_0, t)$. The second key quantity, the distribution function, will be obtained via Liouville mapping, as detailed in the next subsection.

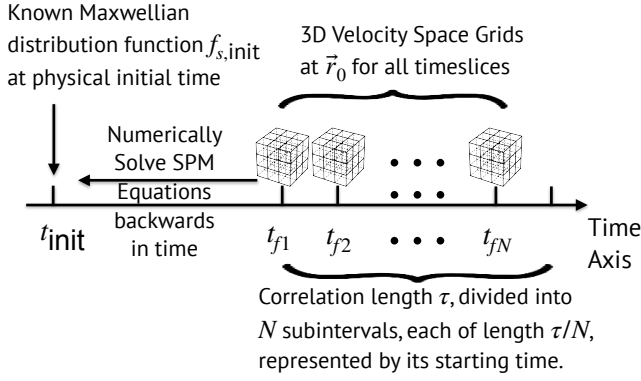


FIG. 1. Illustration of the procedure for Liouville mapping of the velocity distribution function by integrating the single-particle motion (SPM) equations backwards in time from final state $(\mathbf{r}_0, \mathbf{v}, t_f)$ back to initial state $(\mathbf{r}_{\text{init}}, \mathbf{v}_{\text{init}}, t_{\text{init}})$. This procedure must be completed for each of the M points in the 3V velocity-space grid, and for each of the N subintervals that span the correlation interval τ .

C. Liouville Mapping the Distribution Function

To reconstruct $f_s(\mathbf{r}_0, \mathbf{v}, t)$ on a pre-determined velocity space grid suitable for FPC computation, we integrate the single particle motion equations, Eqs. (9) and (10), backward in time, starting from the desired time, t_f . This approach allows us to trace each particle trajectory from the final state $(\mathbf{r}_0, \mathbf{v}, t_f)$ back to its initial state $(\mathbf{r}_{\text{init}}, \mathbf{v}_{\text{init}}, t_{\text{init}})$, when the initial equilibrium velocity distribution function is known. Here we explicitly emphasize that, since we are integrating the particle trajectories backwards in time, the numerical integration begins at t_f and is followed backwards in time to t_{init} .

Specifically, we will compute the distribution function at time t_f based on a known initial equilibrium distribution function $f_{s,\text{init}}(\mathbf{r}_{\text{init}}, \mathbf{v}_{\text{init}}, t_{\text{init}})$. The window function ensures that the electromagnetic field perturbations are zero at t_{init} , so that this initial equilibrium distribution function is uniform in space. In this study, $f_{s,\text{init}}$ is set to be a Maxwellian and thus depends only on velocity. Recall that, to eliminate the oscillatory energy transfer associated with undamped wave motion, the FPC is calculated by a time-average over a chosen correlation interval τ . Therefore, to evaluate FPCs at a spatial location \mathbf{r}_0 and physical time t_0 , the time interval over which we need to determine the distribution function must span the range $t_0 - \tau/2 < t < t_0 + \tau/2$. We require knowledge of the distribution function at the *same position* \mathbf{r}_0 across this time interval on a pre-defined 3V velocity-space grid with M discrete points, $\{\mathbf{v}_{f1}, \mathbf{v}_{f2}, \dots, \mathbf{v}_{fM}, \dots, \mathbf{v}_{fM}\}$.

We divide the time interval into N equal-length subintervals, representing each with its starting time. This yields N sampled time slices $\{t_{f1}, t_{f2}, \dots, t_{fn}, \dots, t_{fN}\}$, with timestep (i.e., the subinterval length) $\Delta t = t_{fn+1} - t_{fn} = \tau/N$. Under this convention, the first time slice is $t_{f1} = t_0 - \tau/2$ and the last is $t_{fN} = t_0 + \tau/2 - \Delta t$. Here, the subscript "f" denotes physical final times for each subinterval.

At the first time slice $t = t_{f1}$, for each velocity grid point

\mathbf{v}_{fm} , we initialize the final state as $(\mathbf{r} = \mathbf{r}_0, \mathbf{v} = \mathbf{v}_{fm})$ and numerically trace the single particle trajectory backward to the initial time t_{init} . This yields $(\mathbf{r}_{\text{init}, m}, \mathbf{v}_{\text{init}, m})$, from which we use Liouville's theorem to obtain

$$f_s(\mathbf{r}_0, \mathbf{v}_{fm}, t_{f1}) = f_{s,\text{init}}(\mathbf{r}_{\text{init}, m}, \mathbf{v}_{\text{init}, m}, t_{\text{init}}). \quad (15)$$

Iterating this process over all M velocity-space points gives the distribution function over the 3V velocity space at $t = t_{f1}$, $f_s(\mathbf{r}_0, \mathbf{v}, t_{f1})$. Next, we advance to t_{f2} , and repeat the above procedure to get $f_s(\mathbf{r}_0, \mathbf{v}, t_{f2})$. The procedure is then repeated at each subsequent time slice t_{fn} , ultimately reconstructing the distribution function over the full time interval, $f_s(\mathbf{r}_0, \mathbf{v}, t_0 - \tau/2 < t < t_0 + \tau/2)$. This procedure for constructing f_s over the full correlation interval τ is illustrated in Fig. 1. Thus, we have obtained the second key quantity, the particle velocity distribution function, needed to compute the FPC, as described in Section II.

D. Computing FPC

With both the electric field and distribution function available from the previous steps, FPCs can be computed. For example, to evaluate $C_{E_{\parallel}, s}(\mathbf{r}_0, \mathbf{v}, t; \tau)$ as defined in Eq. (6), we proceed as follows. At each time slice t_{fn} , the velocity derivative $\partial f_s / \partial v_z$ is computed numerically using a second-order central finite difference scheme for interior points and first-order forward/backward differences at the boundaries of the velocity grid. This derivative is then multiplied by the factor $-q_s v_z^2 / 2$ and the corresponding electric field component $E_z(\mathbf{r}_0, t_{fn})$ to yield the instantaneous contribution to the FPC, i.e. the integrand in Eq. (6). Repeating this calculation across all N time slices within the correlation interval produces a sequence of such contributions, which are then multiplied with the timestep Δt , summed and divided by the interval length τ to obtain the final time-averaged FPC. This process can be similarly applied to other components of the electric field, yielding correlations such as $C_{E_{x,s}}$, $C_{E_{y,s}}$, or $C_{E_{\perp}, s}$, depending on the physics under investigation.

In Fig. 2, we present a flowchart describing the entire procedure, including the field construction, Liouville mapping of the distribution function, and evaluation of the FPC.

E. Caveats

First, in a self-consistent plasma a linear wave damps at the damping rate returned by PLUME, yet our calculation keeps its peak amplitude fixed. This might seem artificial, but in turbulent plasmas, many modes are fed by energy from larger scales, so holding one mode at constant strength is a reasonable assumption. Second, because the electromagnetic wave is pre-defined, we ignore how the particle motion may change the fields. For the small wave amplitude ϵ_l used here, the perturbation to the particle distribution remains weak, so the distribution function's zeroth- and first-order components that set the linear wave frequency and the phase velocity are essentially unchanged. Variations in the fields from the particle

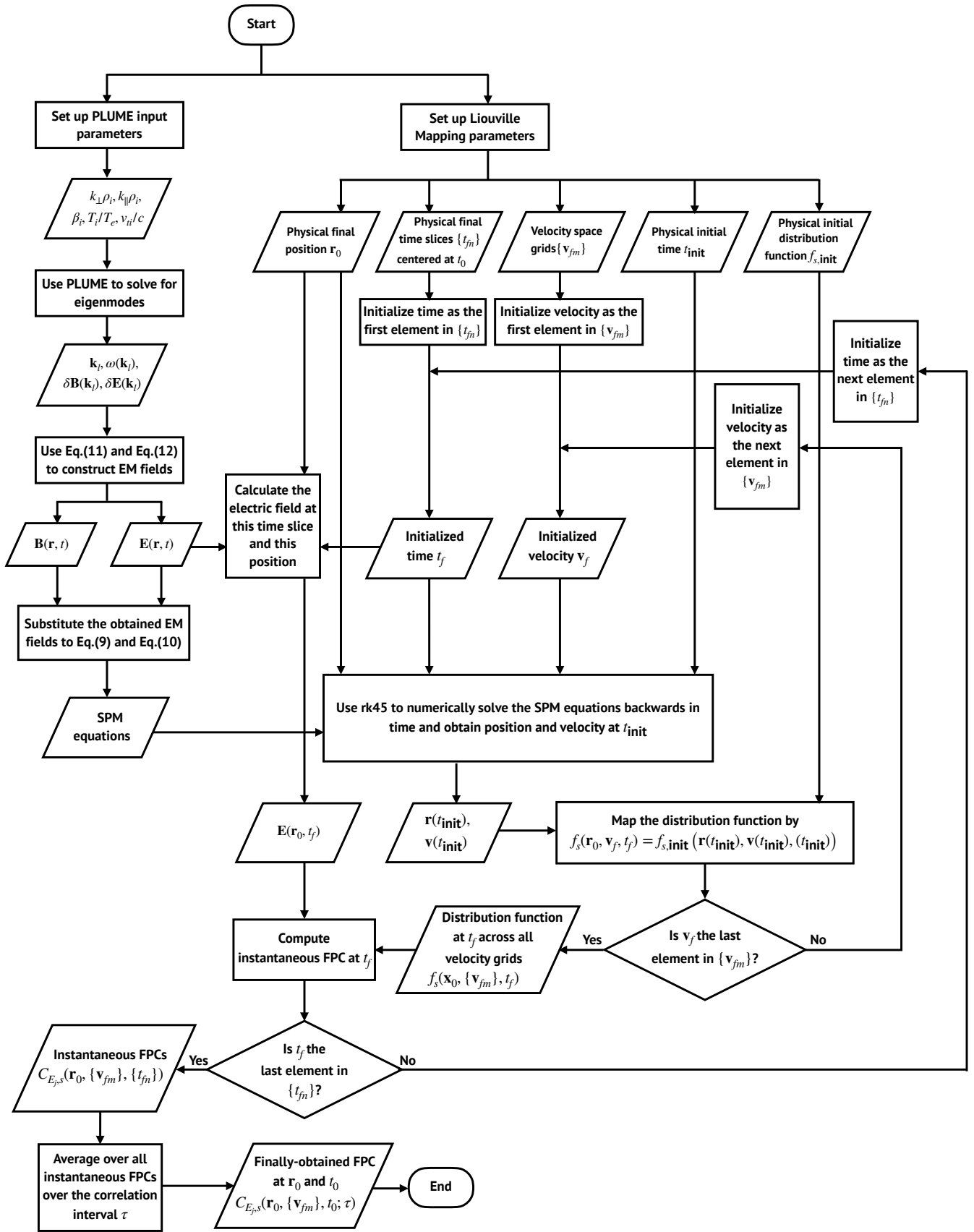


FIG. 2. Flowchart describing the full procedure to construct the electromagnetic fields, perform Liouville mapping of the distribution function, and computation of the FPC, as described in Sec. III. Here, “instantaneous FPCs” refer to the integrands in the definitions of FPCs, i.e. Eq. (4)-(7), and “rk45” denotes the Runge-Kutta-Fehlberg method.

motion appear primarily in the damping rate, not in the wave frequency, leaving the imposed fields qualitatively acceptable to leading order. Third, the approach fully retains nonlinear dynamics: Eqs. (9)–(10) are integrated without approximation, and the Liouville mapping keeps all nonlinear terms in the Vlasov equation. This feature becomes crucial when multiple modes are present. As shown in Appendix B, the FPC signature calculated from the two counter-propagating waves scenario is not a simple superposition of the single-mode results.

IV. RESULTS: LANDAU DAMPING

The velocity-space signature of Landau damping, identified using the FPC technique, has been well established in previous studies^{4,7,13}. A key characteristic of this signature, shown in Figure 6(c) of Klein, Howes, & TenBarge (2017)⁷, is a bipolar pattern centered at the resonant velocity. To validate our method, we compute the FPC from Liouville mapping data, using the electromagnetic fields set according to the eigenfunction for a kinetic Alfvén wave obtained from PLUME, and then we seek the known velocity-space signature of Landau damping.

A. Properties of Kinetic Alfvén Waves

We plot the linear dispersion relation for the kinetic Alfvén wave (KAW) obtained from PLUME for a proton-electron plasma with isotropic equilibrium temperatures for each species and parameters $\beta_i = 1$, $T_i/T_e = 1$, $m_i/m_e = 1836$, $v_{ti}/c = 10^{-4}$, and $k_{\parallel}\rho_i = 0.05$ over the range $10^{-1} \leq k_{\perp}\rho_i \leq 10^1$ in Fig. 3. We plot (a) the wave frequency normalized by the MHD Alfvén wave frequency $\omega/(k_{\parallel}v_A)$ and (b) the normalized total damping rate $|\gamma|/\omega$ (black), ion damping rate $|\gamma_i|/\omega$ (red solid), electron damping rate $|\gamma_e|/\omega$ (blue), and separated damping rate due to ion Landau damping $|\gamma_{i,LD}|/\omega$ (red dashed) as calculated by PLUME^{14,28}, each as a function of $k_{\perp}\rho_i$. The normalized frequency $\omega/(k_{\parallel}v_A) \simeq 1$ in the MHD limit ($k_{\perp}\rho_i \ll 1$), and the electric field polarization²⁵ $\mathcal{P}_E \simeq 0$ indicates linear polarization over the full range plotted, as expected for the KAW.

To determine the electromagnetic field eigenfunctions for a KAW, we choose $k_{\perp}\rho_i = 1$ near the peak in the ion Landau damping rate from PLUME results, as marked by the vertical dashed lines in both panels of Fig. 3. Specifying the wavevector $(k_x\rho_i, k_y\rho_i, k_z\rho_i) = (1, 0, 0.05)$, we obtain the Fourier coefficients of the eigenfunctions $\delta\hat{\mathbf{E}}(\mathbf{k})$ and $\delta\hat{\mathbf{B}}(\mathbf{k})$ and the wave frequency $\omega/\Omega_i = 0.05675$, leading to a period of $T\Omega_i = 110.72$ and a wave phase velocity $\omega/(k_{\parallel}v_{ti}) = 1.135$. For this mode, we choose phase $\alpha = 0$ and set the amplitude scaling factor to $\varepsilon = 0.02$. The time-averaged Poynting vector, $\mathbf{S} = (c/4\pi)\mathbf{E} \times \mathbf{B}$, yields an electromagnetic energy flux for this KAW that is dominantly along the equilibrium magnetic field direction ($+\hat{z}$), with just 3% of the energy flux perpendicular to the magnetic field, so we denote this the *forward-*

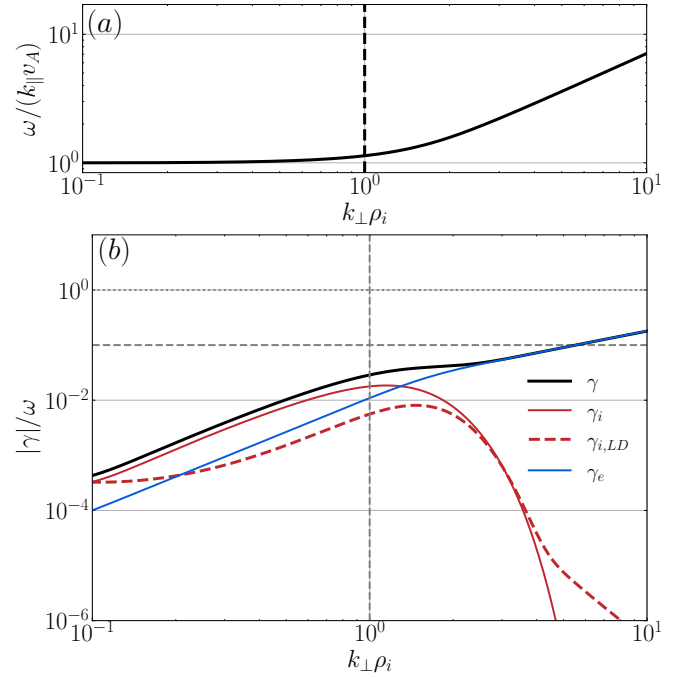


FIG. 3. The normalized (a) frequency $\omega/(k_{\parallel}v_A)$ and (b) damping rates $|\gamma|/\omega$ for a KAW in plasma with parameters $\beta_i = 1$, $T_i/T_e = 1$, $m_i/m_e = 1836$, $v_{ti}/c = 10^{-4}$. The KAW wave mode with $k_{\parallel}\rho_i = 0.05$ is plotted over the range $10^{-1} \leq k_{\perp}\rho_i \leq 10^1$. The damping rates plotted include the total damping rate $|\gamma|/\omega$ (black), ion damping rate $|\gamma_i|/\omega$ (red solid), electron damping rate $|\gamma_e|/\omega$ (blue), and damping rate due to only ion Landau damping $|\gamma_{i,LD}|/\omega$ (red dashed).

propagating wave.

By only changing the sign of the k_z component of the wavevector, giving $(k_x\rho_i, k_y\rho_i, k_z\rho_i) = (1, 0, -0.05)$, we obtain a *backward-propagating wave* with the similar properties except that the parallel-phase velocity flips sign to $\omega/(k_{\parallel}v_{ti}) = -1.135$ and the electromagnetic energy flux for this KAW is primarily along $-\hat{z}$. In our Liouville mapping calculations, in addition to the forward-propagating and backward-propagating KAW cases, we also obtain a *counterpropagating KAW case* by linear superposing both of these solutions, yielding a standing KAW for our case of equal counterpropagating wave amplitudes.

B. Landau damping Signatures with Single Kinetic Alfvén Wave and Two Counter-Propagating Kinetic Alfvén Waves

Next, we compute the gyrotropic parallel FPC, $C_{E_{\parallel}}(v_{\parallel}, v_{\perp})$ ²⁹, for the three cases above: (i) forward-propagating KAW, (ii) backward-propagating KAW, and (iii) counterpropagating KAW cases. For the forward-propagating single-KAW field, we perform Liouville mapping with an initial time of $t_{\text{init}} = -3T$, and calculate the FPC centered at the final time $t_0 = T/2$ over a correlation interval of one wave period, $\tau = T$. The correlation interval is sampled with $N = 40$ time slices, giving a subinterval size of $\Delta t = 0.025T$. The

FPC is computed at the single-point $\mathbf{r}_0/\rho_i = (0.1, 0.1, 0.1)$, but for a correlation interval that samples the full 2π phase of a traveling wave, the resulting FPC is independent of the measurement position.

Because previous studies have shown the the velocity-space signature of ion Landau damping varies primarily in the parallel direction of velocity space, we use Liouville mapping to compute the ion distribution function on a velocity-space grid optimized to extract the expected features. Using cylindrical velocity coordinates (v_\perp, θ, v_z) , we sample the parallel velocity with higher resolution, using 64 equally spaced points over $-3.048 \leq v_z/v_{ti} \leq 3.048$; a lower resolution of 10 points is used to sample the perpendicular coordinate over $0 \leq v_\perp/v_{ti} \leq 3$. The physics of Landau damping is independent of the gyrophase, so we simply choose a single azimuthal slice at $\theta = 0$.

The gyrotropic parallel FPC $C_{E_\parallel}(v_\parallel, v_\perp)$ is plotted in Fig. 4(a), recovering the previously discovered velocity-space signature of ion Landau damping^{5,7,8,30}, providing a validation for our Liouville mapping technique. The bipolar velocity-space signature shows a loss of phase-space energy density (blue) lower than the parallel phase velocity of the wave $\omega/(k_\parallel v_{ti}) = 1.135$ (vertical dashed line) and a gain of phase-space energy density (red) above the parallel phase velocity, consistent with the expected flattening of the velocity distribution function about the phase velocity due to ion Landau damping^{7,30}. With more particles gaining energy than losing it, the net effect is a transfer of energy from the wave to the particles. This bipolar signature is easily observed in the reduced parallel correlation, $C_{E_\parallel}(v_\parallel) = \int C_{E_z}(v_\parallel, v_\perp) dv_\perp$, plotted in Fig. 4(b), where the zero-crossing of the signature is coincident with the parallel phase velocity. Note that for this forward-propagating wave, the resonant velocity lies on the positive side of the velocity space, so the entire signature appears on the right.

For the same Liouville mapping parameters, the backward-propagating KAW case shows a bipolar signature appears at $v_\parallel < 0$ as expected, showing the gyrotropic parallel FPC $C_{E_\parallel}(v_\parallel, v_\perp)$ in Fig. 4(c) and the reduced parallel FPC $C_{E_\parallel}(v_\parallel)$ in Fig. 4(d).

For the counterpropagating KAW case with equal wave amplitudes, the resulting electromagnetic fluctuations yield a standing wave pattern. Since it is the parallel electric field component E_z that mediates the energy transfer in Landau damping²¹, we compute the FPC at a position $z/\rho_i = 31.0$, chosen to coincide with an anti-node of the standing E_z fluctuation. Keeping all other Liouville mapping parameters unchanged, we successfully recover the Landau damping signature at $\mathbf{r}_0/\rho_i = (0.1, 0.1, 31.0)$, as shown in Fig. 4(e) and (f). In this case, we obtain a bipolar signature at both positive and negative parallel velocities, indicating that ions traveling near the phase velocity in both directions resonantly gain energy from the wave when averaged over the correlation interval τ .

Together, the results for the forward-propagating and backward-propagating KAWs and the counterpropagating KAW constitute a thorough validation of our Liouville mapping technique to predict the velocity-space signatures of collisionless damping by the Landau resonance.

V. RESULTS: CYCLOTRON DAMPING

The velocity-space signature of cyclotron damping on the (v_\parallel, v_\perp) plane was first identified by Klein *et al.* (2020)⁵ from turbulence simulation data. Subsequently, Afshari *et al.* (2024)⁶ characterized the features of ion cyclotron damping on the perpendicular (v_x, v_y) plane by modeling the evolution of the distribution function as a Maxwellian distribution centered at the ion bulk flow velocity in the (v_x, v_y) plane. However, Klein *et al.* (2020)⁵ focused solely on turbulent scenarios and did not show how the cyclotron damping signature appears for a single wave mode. While turbulence is more relevant to real-world plasma environments, examining the physics of a single wave mode offers valuable insight into the fundamental physics of ion cyclotron damping. Furthermore, the model in Afshari *et al.* (2024)⁶ is overly simplified and neglects v_z dependence of the velocity-space signature entirely. More importantly, the variation of these ion cyclotron damping signatures with different β_i values has not yet been explored, providing an ideal first science application of the Liouville mapping technique introduced here.

In this section, we address these gaps using our computationally efficient and highly controllable Liouville mapping method. We begin by presenting the properties of selected ion cyclotron wave (ICW) modes from PLUME eigenfunction solutions in Section V A. In Section V B, we reveal the velocity-space signatures of ion cyclotron damping for two single ICW modes with different propagation directions as well as the two counter-propagating ICW modes. The following Sections V C and V D then explain the physical meaning of these signatures. Finally, in Section V E, we examine how these signatures vary with β_i .

A. Properties of Ion Cyclotron Wave modes

For the parameter set $\beta_i = 1$, $T_i/T_e = 1$, $v_{ti}/c = 10^{-4}$, $m_i/m_e = 1836$ and $k_\perp \rho_i = 0.01$, PLUME scans over the range $10^{-2} \leq k_\parallel \rho_i \leq 10^1$ to obtain the linear dispersion relation shown in Fig. 5. We present (a) the wave frequency normalized by the ion cyclotron frequency ω/Ω_i , (b) the electric field polarization \mathcal{P}_E , and (c) the normalized damping rates $|\gamma|/\omega$ as functions of $k_\parallel \rho_i$. In Fig. 5(a), we compare the numerical results for the normalized wave frequency with an analytical approximation (red dashed) based on the cold plasma ion cyclotron wave dispersion relation^{6,31}, here expressed as a function of $k_\parallel \rho_i$ and β_i

$$\frac{\omega}{\Omega_i} = \frac{k_\parallel \rho_i}{2\sqrt{\beta_i}} \left[\sqrt{\left(\frac{k_\parallel \rho_i}{\sqrt{\beta_i}} \right)^2 + 4} - \frac{k_\parallel \rho_i}{\sqrt{\beta_i}} \right] \quad (16)$$

The numerical results show good agreement with this approximation for $k_\parallel \rho_i \ll 1$, where damping remains weak ($-\gamma/\omega < 0.1$). The electric field polarization plot in Fig. 5(b) indicates left-hand circular polarization $\mathcal{P}_E \simeq -1$ for $k_\parallel \rho_i > 0.2$, confirming that this is the ion cyclotron wave solution. The damping rates in Fig. 5(c) reveal that ion damping dominates over

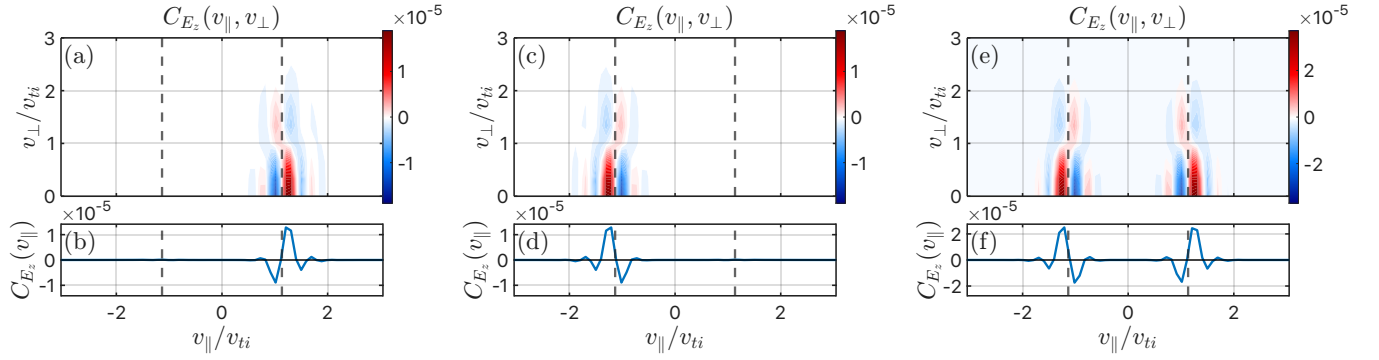


FIG. 4. The gyrotropic parallel FPC $C_{E_z}(v_{\parallel}, v_{\perp})$ (top panels) and reduced parallel FPC $C_{E_z}(v_{\parallel})$ (bottom panels) for (a,b) the forward-propagating KAW case, (c,d) the backward-propagating KAW case, and (e,f) the counterpropagating KAW case, showing bipolar velocity-space signatures arise in the directions corresponding to the wave propagation direction, as expected theoretically.

electron damping over the entire range, with ion cyclotron damping ($\gamma_{i,CD}$, green dashed) dominating for $k_{\parallel}\rho_i \geq 0.2$; we observe that significant ion cyclotron damping ($-\gamma/\omega \geq 0.1$) is expected for $k_{\parallel}\rho_i \geq 0.4$.

To investigate ion cyclotron damping, we select the ICW mode with $k_{\parallel}\rho_i = 0.525$ and $k_{\perp}\rho_i = 0.01$ to construct the electromagnetic field eigenfunctions for a single, forward-propagating ICW using Eqs. (11) and (12). The $k_{\parallel}\rho_i = 0.525$ mode is marked by the vertical dashed line in Fig. 5, which exhibits left-handed polarization and a total damping rate of $-\gamma/\omega = 0.3$, indicating that it is a strongly damped ICW. The corresponding wave frequency is $\omega/\Omega_i = 0.2665$, yielding a normalized wave period of $T\Omega_i = 23.58$. We assign a random phase $\alpha = 0$ to this mode, and set the amplitude scaling factor to $\varepsilon = 0.02$. The Poynting flux for this ICW is primarily along the mean magnetic field in the $+\hat{z}$ direction, with only 1% of the energy flux perpendicular to the mean field.

The electromagnetic eigenfunction for a single, backward-propagating ICW can be generated by choosing all of same parameters except changing the sign of $k_{\parallel}\rho_i = -0.525$, yielding a wave Poynting flux primarily in the $-\hat{z}$ direction. The dispersion characteristics in Fig. 5 remain unchanged under this sign change, and thus are not shown again.

Finally, we generate a standing ICW wave pattern by the linear superposition of these two counterpropagating ICWs with the same amplitude and the same phase $\alpha = 0$ for both modes, denoted the counterpropagating ICW case.

B. Velocity-Space Signatures of the Damping of Single and Counterpropagating Ion Cyclotron Waves

Here we apply the Liouville mapping process to generate the velocity-space signatures of ion cyclotron damping in the forward-propagating, backward-propagating, and counterpropagating ICW cases, as defined in Section V A. For all cases, we set the physical initial time to $t_{\text{init}} = -4T$. The FPC is computed at the spatial point $\mathbf{r}_0/\rho_i = (0.1, 0.1, 0.1)$ and the physical final time $t_0 = T$ over the time interval from 0 to $2T$ with a time step of $\Delta t = 0.025T$. Again, although \mathbf{r}_0 is ex-

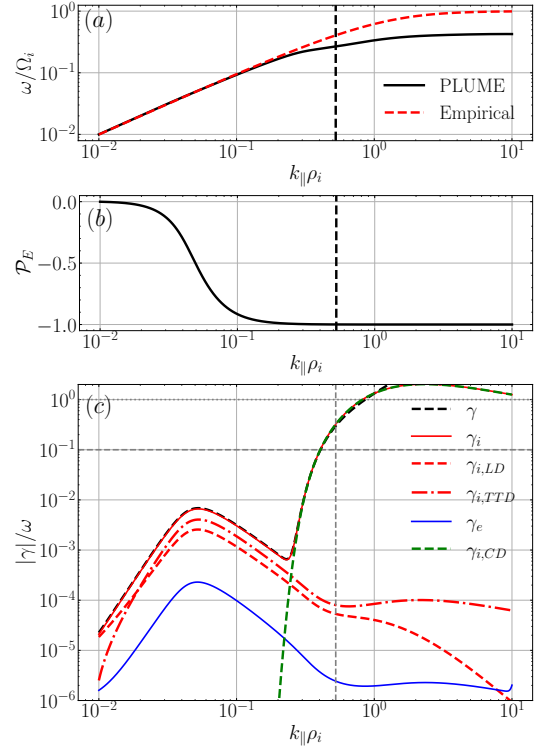


FIG. 5. Linear dispersion relation solution for an ICW from PLUME for plasma parameters $\beta_i = 1$, $T_i/T_e = 1$, $v_{ti}/c = 10^{-4}$, and $m_i/m_e = 1836$. We set the perpendicular component of the wavenumber to $k_{\perp}\rho_i = 0.01$ and present solutions for (a) normalized wave frequency ω/Ω_i (black), (b) electric field polarization \mathcal{P}_E , and (c) normalized damping rates $|\gamma|/\omega$ as a function of $k_{\parallel}\rho_i$. The contributions of ion Landau damping (iLD), ion transit-time damping (iTDD), and ion cyclotron damping (iCD) are separately plotted in (c), showing the rapid and strong onset of ion cyclotron damping as $k_{\parallel}\rho_i \rightarrow 1$. An empirical analytical expression for the cold plasma ICW wave frequency ω/Ω_i (red dashed), given by Eq. (16), is plotted in (a) for comparison.

plicitly specified, the system is spatially homogeneous, so the spatial location does not affect the features of the FPC signatures for the propagating wave cases. Velocity-space grids are set in Cartesian coordinates (v_x, v_y, v_z) , with each dimension spanning from $-4v_{ti}$ to $4v_{ti}$ using 40 sampled points.

In Fig. 6, we present the results of the Liouville mapping for the (a–d) forward-propagating ICW, (e–h) backward-propagating ICW, and (i–l) counterpropagating ICW cases, one in each row. Each column presents (a,e,i) the ion velocity distribution function at the final time slice, (b,f,j) the gyrotropic perpendicular FPC $C_{E_\perp}(v_\parallel, v_\perp)$, and the correlations reduced to the perpendicular plane of velocity space (c,g,k) $C_{E_x}(v_x, v_y)$ and (d,h,l) $C_{E_y}(v_x, v_y)$.

In all cases, FPCs on the perpendicular plane $C_{E_x}(v_x, v_y)$ and $C_{E_y}(v_x, v_y)$ exhibit nearly identical quadrupolar signatures, consistent with those first discovered through the analysis of *MMS* observations of ion cyclotron damping in Earth's turbulent magnetosheath⁶. This pattern arises due to the phase difference between the perpendicular electric field components and the ion bulk velocity in the ion cyclotron wave, as discussed in detail in Section V C.

The plots of the distribution function $f(v_\parallel, v_\perp)$ and the perpendicular FPC $C_{E_\perp}(v_\parallel, v_\perp)$ on the gyrotropic plane, however, are different for these three cases. The normalized parallel wave phase velocity $\omega/(k_\parallel v_{ti})$ of the ICW is labeled with the vertical black dotted line in the gyrotropic plots in the first two columns. The two resonant parallel velocities, solutions of Eq. (1) for the $n = \pm 1$ resonant modes, $v_{\text{res}, n=\pm 1}/v_{ti}$ shown in the gyrotropic plots for the single wave cases, are marked by the two vertical black dashed lines. For the gyrotropic plots of the counterpropagating ICW cases in panels (i) and (j), we plot with vertical black dashed lines only the $n = 1$ resonant velocities for each of the two modes.

For the forward-propagating ICW case, the wave parallel phase velocity is $\omega/(k_\parallel v_{ti}) = 0.508$, with resonant parallel velocities $v_{\text{res}, n=-1}/v_{ti} = 2.413$ and $v_{\text{res}, n=1}/v_{ti} = -1.400$. At the final time plotted in Fig. 6(a), the distribution function shows a shoulder-like extension near the $n = 1$ resonant velocity, as expected theoretically. In contrast, no significant feature appears at the $n = -1$ resonance. This is because cyclotron resonance occurs only when the polarization of the particle's gyromotion matches that of the wave's electric field. In this case, the particles are ions, whose cyclotron motion is left-handed, and the wave is an ICW, which is also left-hand polarized. In the gyrotropic plot of the perpendicular FPC $C_{E_\perp}(v_\parallel, v_\perp)$ in Fig. 6(b), we find a net change of the phase-space energy density associated with the $n = 1$ resonance at $v_{\text{res}, n=1}/v_{ti} = -1.400$, showing a region with a gain of phase-space energy density (red) at $v_\perp > v_{ti}$ above a region of weaker loss of phase-space energy density (blue) at $v_\perp < v_{ti}$. These features represent the time-averaged acceleration of ions in the perpendicular direction due to the perpendicular electric field, as explored in more detail in Section V D.

The backward-propagating ICW case yields a velocity distribution function $f(v_\parallel, v_\perp)$ and perpendicular FPC $C_{E_\perp}(v_\parallel, v_\perp)$ on the gyrotropic plane that looks identical to the forward-propagating ICW case but with the sign of v_\parallel reversed, as would be expected theoretically. Here the paral-

lel wave phase velocity is $\omega/(k_\parallel v_{ti}) = -0.508$, and the resonant velocity for the $n = 1$ mode shifts to $v_{\text{res}, n=1} = 1.400$. For the counterpropagating ICW case, the features of the FPCs $C_{E_x}(v_x, v_y)$ and $C_{E_y}(v_x, v_y)$ on the perpendicular plane are qualitatively similar to the single ICW cases, but with double the amplitude since the two waves are effectively linearly superposed. The gyrotropic perpendicular FPC $C_{E_\perp}(v_\parallel, v_\perp)$ in Fig. 6(j) displays patterns at both $v_z/v_{ti} = -1.400$ and at $v_z/v_{ti} = 1.400$, corresponding to the $n = 1$ resonant velocities of the forward-propagating and backward-propagating ICWs that both contribute to the energization. Note that this velocity-space signature of ion energization is dependent on spatial position for the standing wave pattern, and here we show the result at the position of the anti-node in that pattern. For a detailed discussion of the spatial dependence, see Appendix B.

C. The Quadrupolar Structures of $C_{E_x}(v_x, v_y)$ and $C_{E_y}(v_x, v_y)$

The quadrupolar structures of $C_{E_x}(v_x, v_y)$ and $C_{E_y}(v_x, v_y)$ can be understood using a simplified model based on the linear eigenfunctions computed by PLUME. Focusing on the example of the forward-propagating single-ICW field with $k_\parallel \rho_i = 0.525$, we approximate the ion distribution function as a Maxwellian centered at the bulk flow velocity (U_x, U_y) , obtained from the inverse Fourier transform of the PLUME outputs. While this model neglects v_z dependence, it captures the essential dynamics in the perpendicular velocity plane, where (U_x, U_y) follows a clockwise circular trajectory around the origin, corresponding to the left-hand circular polarization of the ICW. The evolution of (U_x, U_y) (dotted) and (E_x, E_y) (solid) over a full wave period from the PLUME solution for the ICW are plotted in Fig. 7 (a). For the discussion below, we denote the distinct phase angles ϕ_Q for each of these four fields, where $Q = U_x, E_x, U_y, E_y$.

To estimate $C_{E_x}(v_x, v_y)$, consider that its integrand consists of a velocity-space dependent term, $-v_x^2 \partial f / \partial v_x$ and a velocity-space independent term, E_x . For a Maxwellian distribution centered at (U_x, U_y) , the velocity-dependent term produces a bipolar structure: negative to the left of U_x , positive to the right, and zero at the center. When multiplied by E_x , this results in a blue-red bipolar signature (from left to right) centered at U_x for $E_x > 0$ or a red-blue bipolar signature for $E_x < 0$, as shown in Fig. 7(b) at $\omega t/(2\pi) = 0.01$ and (c) at $\omega t/(2\pi) = 0.51$. Here we have set the amplitude by specifying $\varepsilon = 0.5$ for ease of visualization. The same reasoning applies to C_{E_y} with respect to v_y and E_y , shown in Fig. 7(e) and (f).

The quadrupolar patterns in C_{E_x} and C_{E_y} , shown in Fig. 6 (c) and (d), arise from the phase relationships between the ion bulk flow and the electric field components, ϕ_{U_x} , ϕ_{U_y} , ϕ_{E_x} and ϕ_{E_y} . To visualize this, we examine C_{E_x} at four evenly spaced time slices, $\omega t/(2\pi) = 0.01, 0.26, 0.51, 0.76$, during the wave period. Among these, the two slices where E_x is at its peak and trough dominate the time-averaged response, since the contributions from the other two selected time slices are zero because $E_x = 0$ at those times. For C_{E_x} , these two dominant

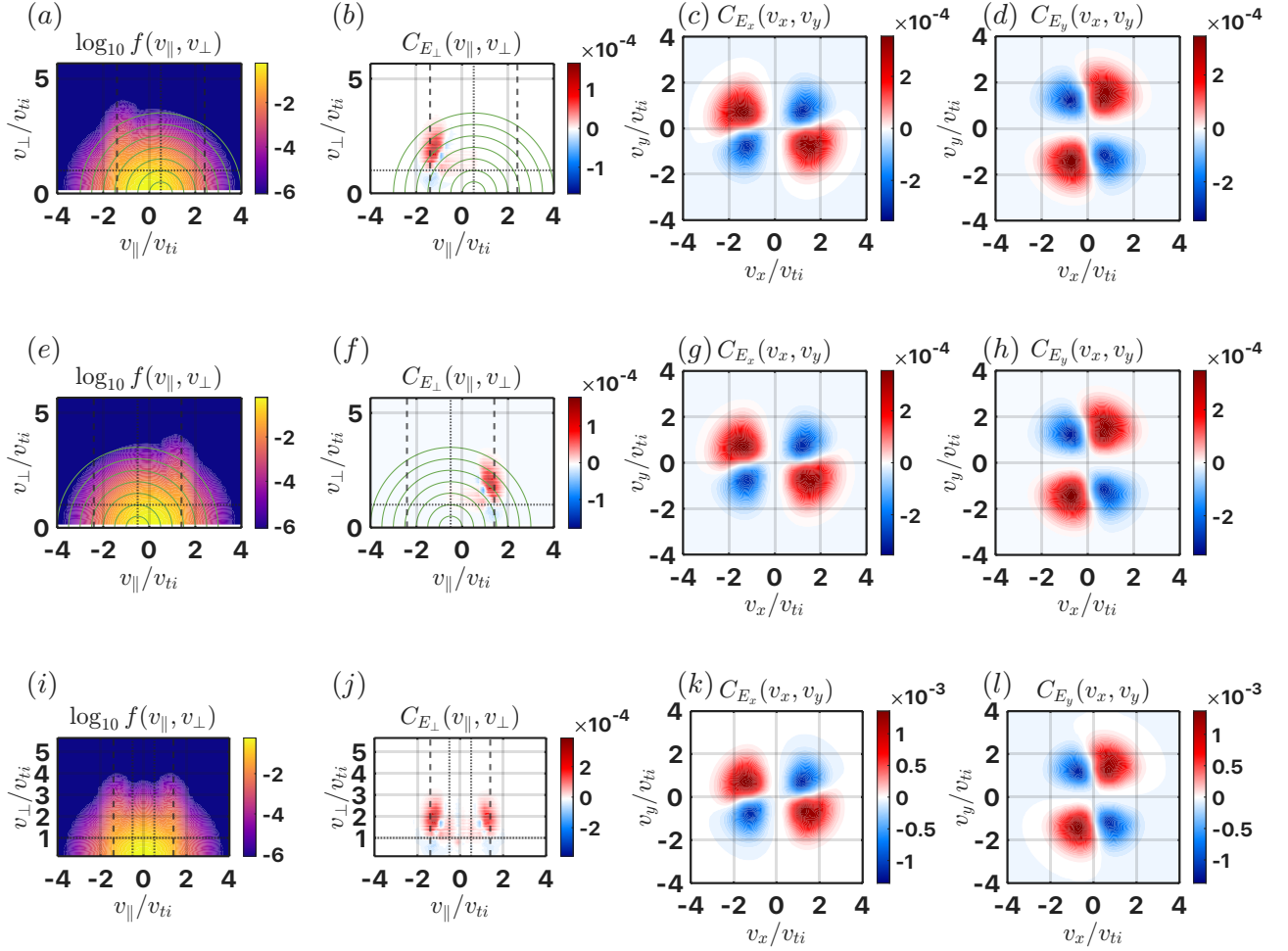


FIG. 6. From our Liouville mapping technique, plots of the (first column) ion velocity distribution function $f(v_{\parallel}, v_{\perp})$ at the final time slice, (second column) gyrotropic perpendicular FPC $C_{E_{\perp}}(v_{\parallel}, v_{\perp})$, (third and fourth columns) FPCs reduced to the perpendicular plane $C_{E_x}(v_x, v_y)$ and $C_{E_y}(v_x, v_y)$ for the (first row, a–d) forward-propagating ICW with $k_{\parallel}\rho_i = 0.525$, (second row, e–h) backward-propagating ICW with $k_{\parallel}\rho_i = -0.525$, and (third row, i–l) counterpropagating ICWs with $k_{\parallel}\rho_i = \pm 0.525$.

snapshots are marked in Fig. 7(a) with vertical black dashed lines. As shown in the second row of Fig. 7, at each time slice, the bulk perpendicular flow velocity $(U_x/v_{ti}, U_y/v_{ti})$ is marked with a star, while a surrounding circle with a radius of one thermal velocity represents the ion distribution along its clockwise gyrating motion around the velocity-space origin. At $\omega t/(2\pi) = 0.01$, where $E_x > 0$, the resulting blue-red dipole appears in the lower half of the (v_x, v_y) plane with $U_x \gtrsim 0$ and $U_y < 0$. At $\omega t/(2\pi) = 0.51$, where $E_x < 0$, the pattern reverses, appearing as a red-blue dipole in the upper half of the plane with $U_x \lesssim 0$ and $U_y > 0$. Summing these two dominant patterns yields the composite shown in Fig. 7(d). This sum effectively represents the time-averaged C_{E_x} over one wave period and reproduces qualitatively the quadrupolar pattern seen in Fig. 6(c).

Analogously for C_{E_y} , the two dominant time slices now occur at $\omega t/(2\pi) = 0.26$ and 0.76 , as labeled by vertical

red dashed lines in Fig. 7(a). The red-blue (from bottom to top) bipolar signature of C_{E_y} at $\omega t/(2\pi) = 0.26$ is shown in Fig. 7(e) and the blue-red signature at $\omega t/(2\pi) = 0.76$ in (f), with their summing in (g) clearly qualitatively reproducing the quadrupolar pattern of C_{E_y} seen in Fig. 6(d).

In summary, the quadrupolar structures of $C_{E_x}(v_x, v_y)$ and $C_{E_y}(v_x, v_y)$ originate from phase differences between the electric field and the ion bulk flow velocity components, which is evident by approximating the evolving distribution as a Maxwellian centered at (U_x, U_y) . Note that this model neglects distortions in (v_x, v_y) plane and any dependence on v_z . Next, we explore the variation of the gyrotropic FPC $C_{E_{\perp}}(v_{\parallel}, v_{\perp})$ as a function of v_z .

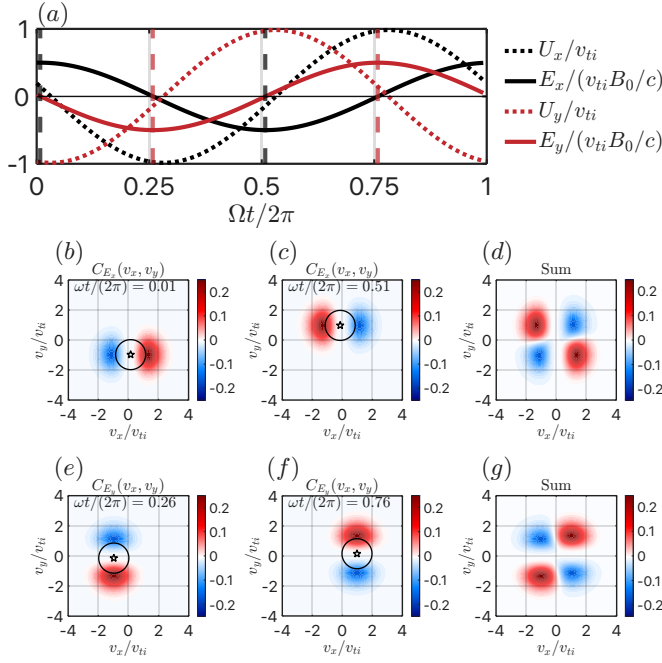


FIG. 7. From PLUME solutions of the ICW eigenfunction, we plot (a) the perpendicular bulk flow velocity components U_x/v_{ti} (black dotted) and U_y/v_{ti} (red dotted) and the perpendicular electric field components $E_x/(v_{ti}B_0/c)$ (black solid) and $E_y/(v_{ti}B_0/c)$ (red solid). The dominant timeslices of C_{E_x} at (b) $\omega t/(2\pi) = 0.01$ and (c) 0.51 combine to produce (d) the quadrupolar velocity-space signature of C_{E_x} , and the timeslices of C_{E_y} at (e) $\omega t/(2\pi) = 0.26$ and (f) 0.76 combine to produce (g) the quadrupolar velocity-space signature of C_{E_y} .

D. The Ion Energization in the Gyrotropic Velocity-Space Signature $C_{E_x}(v_{\parallel}, v_{\perp})$

To understand the features of the gyrotropic FPC $C_{E_{\perp}}(v_{\parallel}, v_{\perp})$, we examine single particle motion trajectories in the gyrotropic plane for the forward-propagating ICW. In Fig. 8, we show six such ion trajectories, each evolving over six wave periods. All ions start from the same spatial position $\mathbf{r} = (0.1, 0.1, 0.1)\rho_i$, with identical initial perpendicular velocity $v_{x0}/v_{ti} = 1$ and $v_{y0}/v_{ti} = 0$. Their initial parallel velocities are: $v_{z0}/v_{ti} = -2.400$ (blue), -1.400 (red), -0.400 (yellow), 1.413 (purple), 2.413 (green), and 3.413 (cyan). The initial parallel velocities of the red and green trajectories correspond to the $n = 1$ and the $n = -1$ resonant velocities (vertical dashed lines), respectively. Dots and stars mark their initial and final velocity-space positions on the gyrotropic plane, respectively.

To visualize how the energy of the ions evolves in the ICW fields, we overlay two sets of semicircles in Fig. 8: gray contours represent constant energy in the lab frame, while black contours represent constant energy in the frame moving at the parallel phase velocity of the ICW (hereafter referred as the ICW frame). Comparing initial and final velocity-space

positions reveals that only the red trajectory, starting at the $n = 1$ resonant velocity ($v_{z0}/v_{ti} = v_{res,n=1}/v_{ti} = -1.400$), experiences significant energy gain. The other five trajectories remain close to their respective initial energy contours.

All ions undergo left-hand polarized cyclotron motion around the background magnetic field $\mathbf{B}_0 = B_0\hat{z}$. Although this lowest-order motion is not visible in the gyrotropic plane as the azimuthal angle is averaged out, it does not contribute to energy gain and therefore does not affect our analysis of energization. The higher-order dynamics, which are responsible for net energy gain, are captured in the red trajectory.

The first of these is pitch angle scattering, where the particle moves along the black semicircle. In the ICW frame, this motion redistributes kinetic energy between parallel and perpendicular components without changing the total velocity. In the lab frame, however, the total velocity increases as the pitch angle in the ICW frame decreases, and vice versa. This effect is visible in Fig. 8 with the aid of the gray semicircles, i.e. the constant energy contours in the lab frame. Given a Maxwellian velocity distribution centered at the origin, more particles tend to occupy large pitch angles in the ICW frame than small ones. As a result, more particles gain energy than lose it, leading to a net transfer of energy from the electromagnetic fields to the particles.

The red trajectory also shows a slow outward drift perpendicular to the energy contour in the ICW frame. Unlike pitch-angle scattering, which does not result in energy gain in the ICW frame and only leads to energization in the lab frame by relying on the fact that the number of particles gaining energy exceeds those losing energy, this outward drift represents an energy gain in both the ICW and lab frames for each ion individually.

Together, pitch-angle scattering and outward drift to higher energy result in a net energy gain along the positive v_{\perp} direction. This is the key dynamics underlying the upward red lobe in $C_{E_{\perp}}(v_{\parallel}, v_{\perp})$, as captured by FPC shown in Fig. 6(b). This indicates an increasing probability of finding particles after the system has evolved for $5T$ with $v_{\parallel} \sim v_{res,n=1}$ and $v_{\perp} > v_{ti}$, and the consequent decreasing probability for particles with $v_{\parallel} \sim v_{res,n=1}$ and $v_{\perp} < v_{ti}$ (required for conservation of particle number).

In summary, the velocity-space signature of ion cyclotron damping is characterized by the perpendicular gyrotropic velocity-space signature $C_{E_{\perp}}(v_{\parallel}, v_{\perp})$ in Fig. 6(b) along with the two perpendicular plane signatures $C_{E_x}(v_x, v_y)$ and $C_{E_y}(v_x, v_y)$ in Fig. 6(c) and (d). These signatures are consistent with the previous observational identification using *MMS* observations in Earth's turbulent magnetosheath plasma⁶.

E. Variation of the Velocity-Space Signature of Ion Cyclotron Damping with β_i

Here we use Liouville mapping to investigate how the velocity-space signature of ion cyclotron damping varies with ion plasma beta β_i . To have an overall sense of the properties of the ICW as β_i varies, we use PLUME to solve for the linear

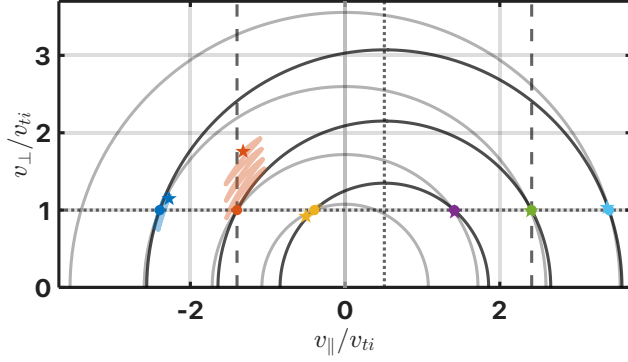


FIG. 8. Selected single ion trajectories in the forward-propagating ICW fields with $k_{\parallel}\rho_i = 0.525$ on the gyrotropic $(v_{\parallel}, v_{\perp})$ plane. The vertical black dotted line labels the wave parallel phase velocity $\omega/(k_{\parallel}v_{ti}) = 0.508$, and the two vertical black dashed lines mark the two resonant velocity $v_{\text{res},n=-1}/v_{ti} = 2.413$ and $v_{\text{res},n=1}/v_{ti} = -1.400$. Initial velocities (dots) and final velocities (stars) are indicated.

dispersion relation of ICWs over the two-dimensional parameter space $(k_{\parallel}\rho_i, \beta_i)$, covering the ranges $0.1\sqrt{0.1} \leq k_{\parallel}\rho_i \leq 10\sqrt{10}$ and $0.1 \leq \beta_i \leq 10$. We hold constant the parameters $k_{\perp}\rho_i = 0.01$, $T_i/T_e = 1$, $v_{ti}/c = 10^{-4}$ and $m_i/m_e = 1836$. In Fig. 9(a), we plot a colormap of the normalized total damping rate, $-\gamma/\omega$, on a logarithmic scale, with black dashed contours denoting $-\gamma/\omega = 10^{-4}, 10^{-3}, \dots, 10^3$. The $-\gamma/\omega = 1$ contour is highlighted in solid blue, which appears nearly vertical and closely follows the $k_{\parallel}\rho_i = 0.8$ grid line. This contour effectively divides the parameter space: on the left are more weakly damped ICWs with $-\gamma/\omega < 1$, and on the right ICWs are extremely strongly damped, decaying within a fraction of a wave period when $-\gamma/\omega > 1$. Since our Liouville mapping approach assumes constant amplitude (rather than decaying) wave fields, we restrict our application of the technique to parameter choices within the $-\gamma/\omega < 1$ region.

As discussed in Section V, a key feature of the gyrotropic FPC $C_{E_{\perp}}(v_{\parallel}, v_{\perp})$ is the localization of the net ion energization near the $n = 1$ resonant velocity. To examine how this resonant velocity varies with β_i , we plot $v_{\text{res},n=1}/v_{ti}$ over the $(k_{\parallel}\rho_i, \beta_i)$ plane in Fig. 9(b). We set the lower limit of the color bar to -3 , as values with $v_{\text{res},n=1}/v_{ti} < -3$ yield extremely weak ion cyclotron damping rates. This is because the Maxwellian velocity distribution contains very few particles in velocity-space regions far from the origin.

Notably, within the $-\gamma/\omega < 1$ region, the contours of $v_{\text{res},n=1}/v_{ti}$ in Fig. 9(b) remain nearly vertical, indicating a weak dependence of the resonant velocity on β_i . To understand this behavior, we rewrite the resonance condition from Eq. (1) to express $v_{\text{res},n}/v_{ti}$ in terms of β_i and $k_{\parallel}\rho_i$,

$$\frac{v_{\text{res},n}}{v_{ti}} = \frac{1}{k_{\parallel}\rho_i} \left(\frac{\omega}{\Omega_i} - n \right) \quad (17)$$

At first glance, there appears to be no β_i dependence in this expression. However, the normalized wave frequency ω/Ω_i

β_i	$-\gamma/\omega$	$v_{\text{res},n=1}/v_{ti}$	ω/Ω_i	$T\Omega_i$
0.1	0.488	-0.777	0.592	10.613
0.3	0.374	-1.081	0.433	14.526
1	0.298	-1.400	0.267	23.575
3	0.275	-1.618	0.151	41.672
10	0.293	-1.773	0.0693	90.662

TABLE II. For $k_{\parallel}\rho_i = 0.525$ and the five β_i values, the resulting PLUME solutions for normalized damping rate $-\gamma/\omega$, resonant velocity $v_{\text{res},n=1}/v_{ti}$, wave frequency ω/Ω_i , and wave period $T\Omega_i$.

does depend on β_i in a nontrivial way, as shown in Fig. 9(c). Since we are analyzing the $n = 1$ resonance condition, this plot essentially represents the ratio of the first term (ω/Ω_i) to the second term ($n = 1$) inside the parentheses in Eq. (17). At $\beta_i \gtrsim 1$, the resonant velocity is dominated by second term ($n = 1$), while at $\beta_i < 1$, a weak dependence on β_i emerges. However, even for the $\beta_i = 0.1$ case where $\omega/\Omega_i \simeq 0.65$ crossing the contour of $-\gamma/\omega = 1$ (solid blue line), the second term still dominates (nearly twice of the first), so the effect of the β_i dependence remains weak.

Finally, in Fig. 9(d) we plot the electric field polarization for the ICW mode over the $(k_{\parallel}\rho_i, \beta_i)$ parameter space, showing a value $\mathcal{P}_E = -1$ across most of the parameter plane. This plot confirms the left-hand circularly polarized electric field theoretically expected for ICWs.

Given the weak dependence on β_i of the ICW properties shown in Fig. 9, we fix $k_{\parallel}\rho_i = 0.525$ and select five representative β_i values, $\beta_i = 0.1, 0.3, 1, 3, 10$, marked with black dots in all panels of Fig. 9. For these five parameter choices, the corresponding values of normalized damping rate $-\gamma/\omega$, resonant velocity $v_{\text{res},n=1}/v_{ti}$, wave frequency ω/Ω_i , and wave period $T\Omega_i$ from the PLUME solutions are summarized in Table II. Two important trends emerge from Table II: (i) the normalized ICW mode period, $T\Omega_i$, increases significantly with β_i ; and (ii) the magnitude of $v_{\text{res},n=1}/v_{ti}$ only increases modestly, from -0.777 at $\beta_i = 0.1$, to -1.773 at $\beta_i = 10$.

For the five β_i choices in Table II, we use Liouville mapping to predict the velocity-space signatures of ion cyclotron damping in the same format as Fig. 6. For all cases, the physical initial time is set to $t_{\text{init}} = -4T$, and the FPC is computed over a correlation interval $0 < t_f < 2T$. The resulting velocity-space signatures are presented in Fig. 10, with the β_i in each row increasing from top to bottom.

Although the velocity-signature reduced to the perpendicular plane $C_{E_x}(v_x, v_y)$ (third column) and $C_{E_y}(v_x, v_y)$ (fourth column) differ quantitatively (such as amplitude and overall shape of the quadrupolar pattern), the qualitative quadrupolar pattern remains unchanged as β_i varies: for C_{E_x} , red lobes appear in quadrants II and IV; and for C_{E_y} , in quadrants I and III.

For the gyrotropic velocity-space signatures $C_{E_{\perp}}(v_{\parallel}, v_{\perp})$ (second column), the signature remains well-localized near $v_{\text{res},n=1}$ (leftmost vertical dashed line) across all β_i cases. In addition, the zero-crossing from loss of phase-space energy density (faint blue) to gain of phase-space energy density (red) occurs at $v_{\perp} \sim v_{ti}$, independent of β_i .

A noticeable trend in Fig. 10 is that, as β_i increases, the distribution function $f(v_{\parallel}, v_{\perp})$ (first column) and gyrotropic velocity-space signature $C_{E_{\perp}}(v_{\parallel}, v_{\perp})$ (second column) become increasingly extended to higher v_{\perp} values. This variation is a consequence of our implementation of the Liouville mapping technique and the strong variation of wave period $T\Omega_i$ as a function of β_i , as shown in Table II. Although the physical initial time is consistently set relative to the wave period to $-4T$, ensuring each system evolves for four ICW wave periods before computing the FPC, the absolute value of the normalized ICW mode period $T\Omega_i$ increases significantly with β_i . At $\beta_i = 0.1$, the system evolves for $4T\Omega_i = 42.452$ before the computation of FPC on the correlation interval of $\tau\Omega_i = 21.22$; in contrast, at $\beta_i = 10$, these values increase to $4T\Omega_i = 362.648$ and $\tau\Omega_i = 181.324$. We present a direct comparison of cases with matched absolute evolution time and correlation interval for different β_i values in Appendix A.

In summary, our general prediction from this study is that the velocity space signatures of ion cyclotron damping do not vary qualitatively with β_i , except for the relatively weak quantitative change in the $n = 1$ resonant velocity, $v_{\text{res}, n=1}$.

VI. CONCLUSION

Resonant wave-particle interactions are fundamental mechanisms responsible for the collisionless damping of electromagnetic waves in plasmas. The field-particle correlation (FPC) technique has proven to be an effective tool for characterizing these interactions by revealing their distinctive velocity-space signatures of particle energization. While the $n = 0$ Landau resonance has been extensively studied (including the identification of its velocity-space signatures for both ions^{3,4,7} and electrons¹³, the physical interpretation of these signatures³, their dependence on plasma parameters^{13,14}, and their detection in numerical simulations¹⁰, spacecraft observations^{11,12}, and laboratory experiments²¹), cyclotron damping via the $n = \pm 1$ resonances remains less thoroughly explored. This situation is largely due to the challenge of obtaining well-controlled data where cyclotron damping dominates over other energization processes.

This study addresses two key gaps: (1) the lack of a computationally efficient method for generating well-controlled data, and (2) limited understanding of the physics underlying ion cyclotron damping. We fill the first gap using the Liouville mapping method and the second by systematically using Liouville mapping with the FPC technique to characterize the velocity-space signatures of ion cyclotron damping.

The Liouville mapping method is based on Liouville's theorem, which states that the distribution function remains constant along particle trajectories in phase space. In plasma physics, this corresponds to solving the Vlasov equation implicitly by numerically solving the equations of motion for individual particles.

We integrate this approach with the FPC framework using the procedure illustrated in Fig. 2, with several caveats. The electromagnetic fields are analytically specified from eigenfunctions obtained using solutions to the linear Vlasov-

Maxwell dispersion relation. Although we neglect the collisionless damping of the electromagnetic fields of the waves by assuming a fixed peak amplitude in time and ignore the self-consistent distortions to the fields from particle motion, both of which make the system non-self-consistent, we argue in Section III E that this approximation is reasonable for qualitatively predicting the velocity-space signatures of collisionless damping of the waves.

We validate our method by recovering the known velocity-space signatures of Landau damping from our Liouville mapping approach with single propagating and standing KAWs, as shown in Fig. 4. We then apply the technique to ICWs and investigate the velocity-space signatures of ion cyclotron damping with unprecedented details.

This study yields several key findings about velocity-space signature of ion cyclotron damping. First, ion cyclotron damping produces a quadrupolar pattern in the (v_x, v_y) plane, driven by the phase relations between the ion bulk flow and the perpendicular electric field. This behavior can be intuitively understood by modeling the motion of the ion distribution as a Maxwellian centered at the bulk flow velocity, as detailed in Fig. 7. Second, ion cyclotron damping leads to net ion energization to higher v_{\perp} near the $n = 1$ resonant parallel velocity in the $(v_{\parallel}, v_{\perp})$ plane, driven by pitch-angle scattering and acceleration to higher energy, both in the frame of the ion cyclotron wave. This process is revealed by examining single-particle trajectories in the $(v_{\parallel}, v_{\perp})$ plane, as visualized in Fig. 8. Third, these features remain largely unchanged across a broad range of ion plasma values, $\beta_i = 0.1, 0.3, 1, 3, 10$, as shown in Fig. 10. To isolate the influence of β_i , we fix the parallel wavenumber at $k_{\parallel}\rho_i = 0.525$. This choice is motivated by the finding that the $n = 1$ resonant velocity depends only weakly on β_i and is instead primarily determined by $k_{\parallel}\rho_i$, as shown in Fig. 9.

To our knowledge, this work presents the first detailed characterization of how ion cyclotron damping velocity-space signatures vary with β_i . These results offer valuable benchmarks for identifying ion cyclotron damping in spacecraft observations and provide a methodical foundation for future studies of other wave-particle interactions.

ACKNOWLEDGMENTS

R. Huang thanks Daniel J. McGinnis for inspiring discussions. This work was supported by NASA Award 80NSSC24K1241.

DATA AVAILABILITY STATEMENT

The data and code that support the findings of this study are openly available in Zenodo at <http://doi.org/10.5281/zenodo.16541375>, reference number [32].

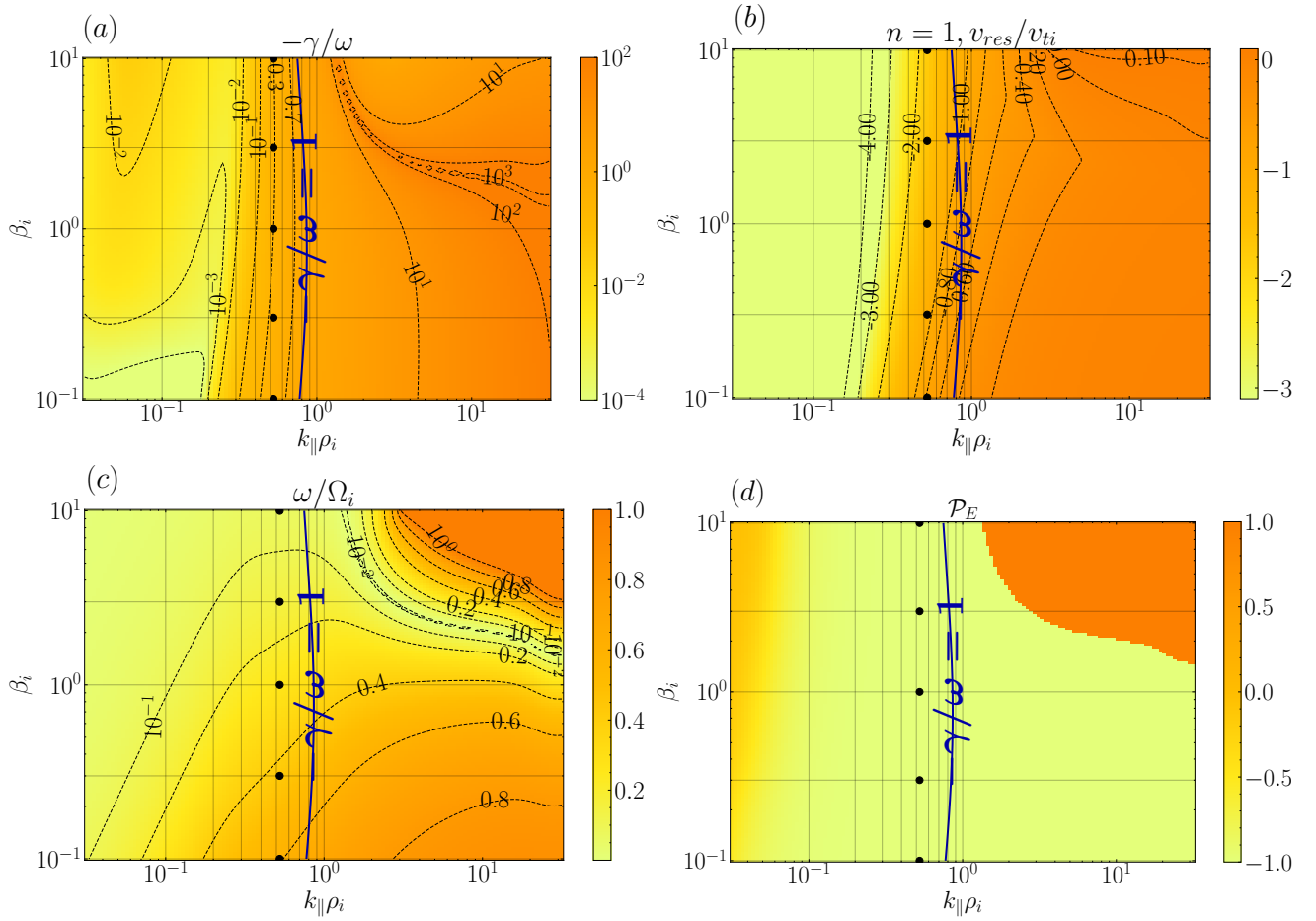


FIG. 9. For plasma parameters $T_i/T_e = 1$, $v_{ti}/c = 10^{-4}$ and $m_i/m_e = 1836$ and perpendicular wavenumber $k_{\perp}\rho_i = 0.01$, PLUME solutions on the $(k_{\parallel}\rho_i, \beta_i)$ parameter space for the (a) normalized damping rate $-\gamma/\omega$, (b) $n = 1$ mode resonant velocity $v_{res, n=1}/v_{ti}$, (c) normalized wave frequency ω/Ω_i , and (d) electric field polarization \mathcal{P}_E . The chosen ICW modes at $\beta_i = 0.1, 0.3, 1, 3, 10$ are labeled as five black dots on each panel.

Appendix A: Dependence of Ion Cyclotron Damping Signatures on System Evolution Duration

As mentioned at the end of Section V E, to verify whether the increasing deformation of the distribution function and the expansion of FPCs to higher v_{\perp} in Fig. 10 with increasing β_i is driven by the absolute system evolution time, we conduct two additional tests. By adjusting the system evolution time $t\Omega_i$ before the FPC correlation interval begins and the FPC correlation interval $\tau\Omega_i$, we can compare these new cases to previously calculated cases with similar values of $t\Omega_i$ and $\tau\Omega_i$. We present these values for two new comparisons in Table III.

In Fig. 11, we present a comparison between the new $\beta_i = 0.1$ case in the first row of Table III and the old $\beta_i = 1$ case from the top row of Fig. 6. With the longer absolute integration time and correlation interval, the gyrotropic signature in Fig. 11(b) for $\beta_i = 0.1$ looks much more qualitatively and quantitatively similar to the $\beta_i = 1$ case in (f). The perpendicular signatures for $\beta_i = 0.1$ in (c, d) also look more quantitatively similar to the $\beta_i = 1$ case in (g, h).

In Fig. 12, we present a comparison between the new $\beta_i = 10$ case in the third row of Table III and the old $\beta_i = 3$ case from the fourth row of Fig. 10. With the shorter absolute integration time and correlation interval, the gyrotropic signature in Fig. 12(b) and the perpendicular signatures in (c, d) for $\beta_i = 10$ no longer extend to the much higher v_{\perp} values observed in Fig. 10(q–t), looking much more quantitatively similar to the $\beta_i = 3$ case in Fig. 12(f–h).

Together the results from Figs. 11 and 12 support our hypothesis that the most striking differences, particularly in the ion cyclotron damping gyrotropic signatures, disappear when their absolute Liouville mapping calculation times are matched with those of the previous beta = 1 and 3 cases. This analysis reinforces the prediction from Section V E that the velocity space signatures of ion cyclotron damping do not vary significantly with variations in β_i .

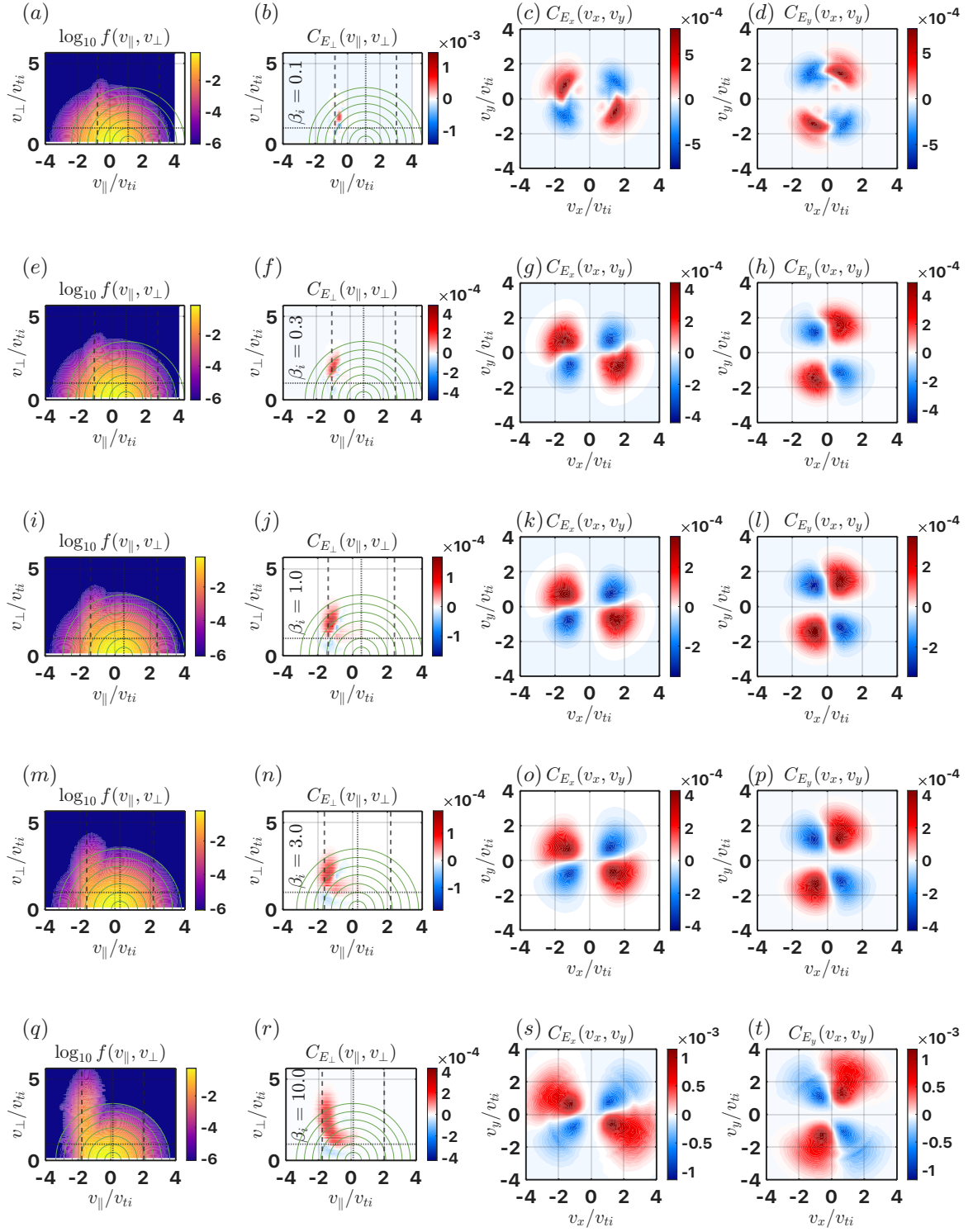


FIG. 10. The ion velocity distribution function $f(v_{\parallel}, v_{\perp})$, gyrotropic perpendicular FPC $C_{E_{\perp}}(v_{\parallel}, v_{\perp})$, and FPCs reduced to the perpendicular plane $C_{E_x}(v_x, v_y)$ and $C_{E_y}(v_x, v_y)$, in the same format as Fig. 6. From top to bottom, rows present the results for $\beta_i = 0.1, 0.3, 1, 3, 10$.

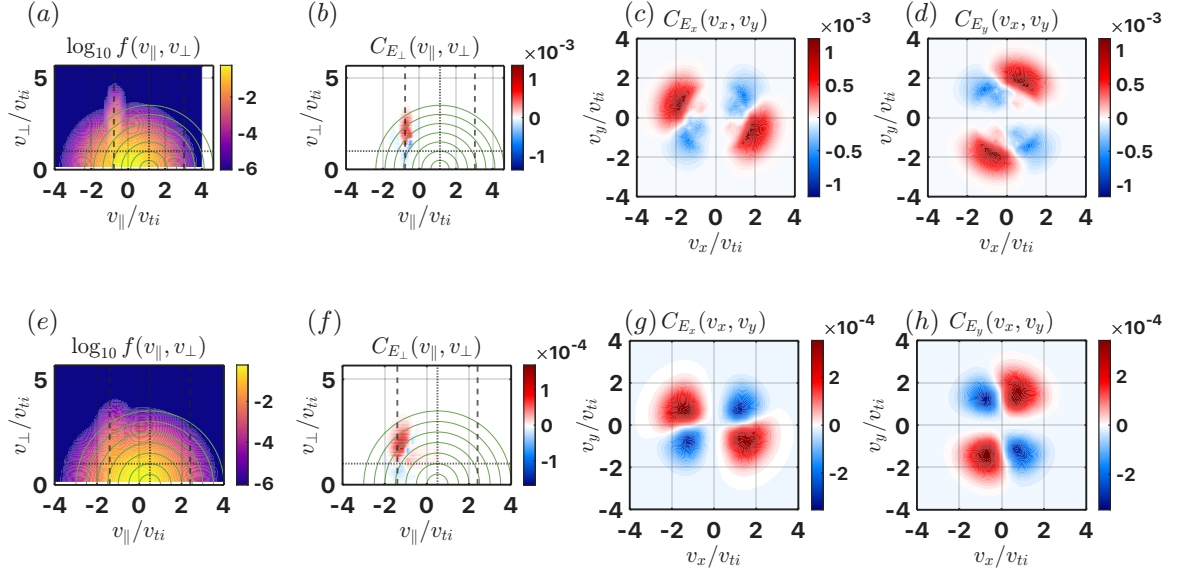


FIG. 11. Comparison of the velocity-space signatures of ion cyclotron damping between the $\beta_i = 0.1$ and $\beta_i = 1$ cases when the system evolution time $t\Omega_i$ and correlation interval $\tau\Omega_i$ have similar absolute times, as presented in the first two rows of Table III.

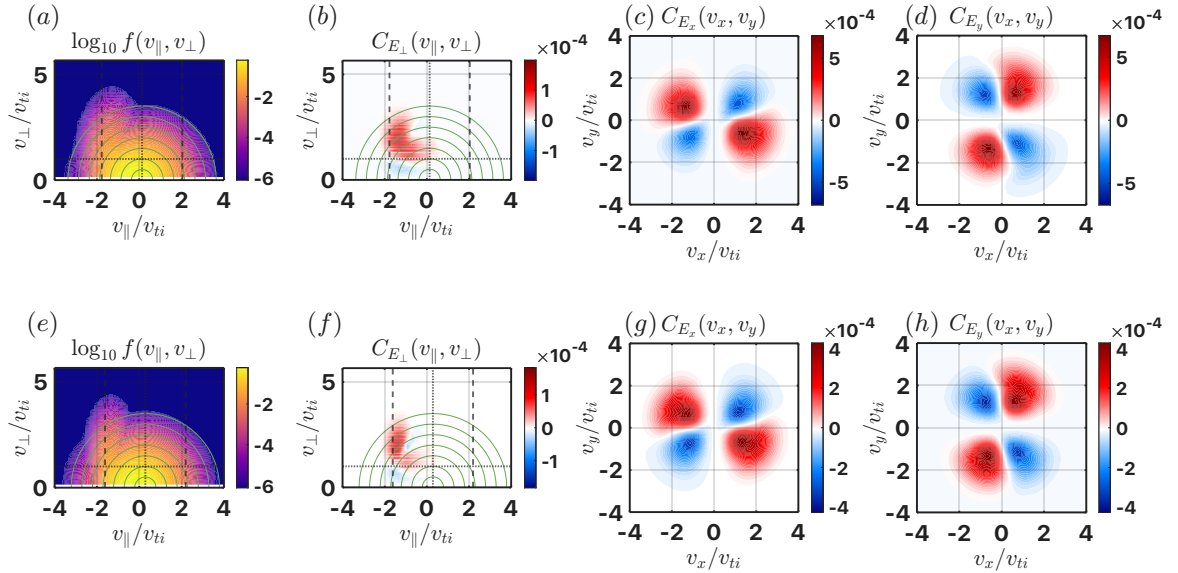


FIG. 12. Comparison of the velocity-space signatures of ion cyclotron damping between the $\beta_i = 10$ and $\beta_i = 3$ cases when the system evolution time $t\Omega_i$ and correlation interval $\tau\Omega_i$ have similar absolute times, as presented in the last two rows of Table III.

Appendix B: Asymmetry in the Gyrotropic Velocity-Space Signature of Ion Cyclotron Damping with Two Counter-propagating ICWs

Revisiting ion cyclotron damping signatures in Fig. 6, it is tempting to predict that, in the case of the standing ICW fields constructed by superposing two counter-propagating ICWs,

the resulting gyrotropic FPC signature would simply be the linear superposition of the individual signatures from each single mode. As shown in Fig. 6, a single propagating ICW produces a signature on one side (with either $v_{\parallel} > 0$ or $v_{\parallel} < 0$) of the gyrotropic velocity plane (near the $n = 1$ resonant velocity of this ICW), while the counterpropagating ICW case yields patterns on both sides, corresponding to the $n = 1$ res-

β_i	t_{init}	Interval	$t\Omega_i$	$\tau\Omega_i$
0.1	$-9T$	$[0, 5T]$	95.517	53.065
1	$-4T$	$[0, 2T]$	94.300	47.150
10	$-2T$	$[0, T]$	181.324	90.662
3	$-4T$	$[0, 2T]$	166.688	83.344

TABLE III. Tests to compare cases with different β_i (and thus different wave periods) but similar absolute system evolution time before correlation $t\Omega_i$ and correlation interval $\tau\Omega_i$. The new $\beta_i = 0.1$ case (first row of this table) compares to the $\beta_i = 1$ case from Fig. 6(a–d), with the comparison shown in Fig. 11. The new $\beta_i = 0.1$ case (third row of this table) compares to the $\beta_i = 3$ case from Fig. 10(m–p), with the comparison shown in Fig. 12.

onant velocities of the two ICWs. Specifically, the signatures with $v_{\parallel} > 0$ and $v_{\parallel} < 0$ each consist of a red region of increasing phase-space energy density at $v_{\perp} > v_{ti}$ and a more faint blue region of decreasing phase-space energy density at $v_{\perp} < v_{ti}$.

However, as it turns out, the symmetry of the gyrotropic velocity-space signature for counter-propagating ICWs depends on the position of the field-particle correlation analysis within the standing, counter-propagating ICW fields, as shown in Fig. 13. As discussed in Section III E, even though the wave electromagnetic fields are specified from the linear dispersion relation, the Liouville mapping procedure retains nonlinear effects by evolving the distribution function along particle trajectories without dropping nonlinear terms. Thus, the results may not necessarily be interpreted as the sum of purely linear responses. To investigate this further, consider the perpendicular electric field components $E_x(\mathbf{r}, t)$ and $E_y(\mathbf{r}, t)$ generated by two counter-propagating ICWs with wave vectors $\mathbf{k}_{1,2}\rho_i = 0.01\hat{x} \mp 0.525\hat{z}$. From the PLUME solver, the two wave modes have equal frequencies $\omega(\mathbf{k}_1) = \omega(\mathbf{k}_2) \equiv \omega$ and Fourier coefficients for the perpendicular components of the electric field $\delta\hat{E}_{x,y}(\mathbf{k}_1) = \delta\hat{E}_{x,y}(\mathbf{k}_2) \equiv \delta\hat{E}_{x,y}$. Writing the Fourier coefficients in polar form, $\delta\hat{E}_{x,y} = |\delta\hat{E}_{x,y}|e^{i\phi_{E_{x,y}}}$, taking the same wave amplitudes with $\varepsilon_1 = \varepsilon_2 \equiv \varepsilon$, and substituting into Eq. (11) and Eq. (12), we obtain the x - and y -components of the electric field after the first wave period, i.e. once the window function has fully ramped up the amplitude, as follows

$$E_{x,y}(\mathbf{r}, t) = 2\varepsilon|\delta\hat{E}_{x,y}|\cos\left[\frac{(\mathbf{k}_1 + \mathbf{k}_2) \cdot \mathbf{r} - 2\omega t + 2\phi_{E_{x,y}}}{2}\right] \times \cos\left[\frac{(\mathbf{k}_1 - \mathbf{k}_2) \cdot \mathbf{r}}{2}\right]. \quad (\text{B1})$$

For a left-hand polarized ICW, $|\delta\hat{E}_x| = |\delta\hat{E}_y|$ and $\phi_{E_x} - \phi_{E_y} = \pi/2$. This gives a time-independent expression for the perpendicular electric field magnitude

$$E_{\perp}(\mathbf{r}) = \sqrt{E_x^2(\mathbf{r}, t) + E_y^2(\mathbf{r}, t)} \\ = 2\varepsilon|\delta\hat{E}_x|\sqrt{\cos^2\left[\frac{(\mathbf{k}_1 - \mathbf{k}_2) \cdot \mathbf{r}}{2}\right]}, \quad (\text{B2})$$

which varies spatially along z with a wavelength $\lambda_z = 5.984\rho_i$.

As shown in Fig. 13(top), E_{\perp} peaks at $z = 0$ and vanishes at integer multiples of $z = \pm 2.992\rho_i$. To examine how this spatial variation affects the FPC signature, we run Liouville mapping at four evenly spaced z positions, $z/\rho_i = -2.9, -1.4, 0.1, 1.6$, while keeping all other parameters identical to those used in the main text. These positions, marked with black dashed lines in Fig. 13(top), are chosen to avoid the exact node where $E_{\perp} = 0$. The resulting gyrotropic FPCs are shown in the second through fifth rows of Fig. 13.

At $z = 0.1\rho_i$ in Fig. 13(fourth row), near the peak E_{\perp} , the FPC shows a symmetric pattern of ion energization at both $v_{\parallel} > 0$ and $v_{\parallel} < 0$. These patterns are centered near the two $n = 1$ resonant velocities associated with the two counter-propagating wave modes. This symmetric feature indicates that ions resonating with both wave modes are gaining energy.

However, at $z = -2.9\rho_i$ (second row) and $-1.4\rho_i$ (third row), the FPC pattern becomes asymmetric: ions near the $n = 1$ resonance of the backward-propagating wave (\mathbf{k}_1) gain energy, while those near the forward-propagating wave (\mathbf{k}_2) lose energy. At $z = 1.6\rho_i$ (fourth row), this asymmetry is reversed in v_{\parallel} , with ions near the \mathbf{k}_2 resonance gaining energy while those near the \mathbf{k}_1 resonance lose energy. The origin of this asymmetry is unclear, and will require further investigation. We suspect that the asymmetry results from nonlinear effects captured by the Liouville mapping method.

¹K. H. Kiyani, K. T. Osman, and S. C. Chapman, “Dissipation and heating in solar wind turbulence: from the macro to the micro and back again,” *Philosophical Transactions of the Royal Society A: Mathematical, Physical and Engineering Sciences* **373**, 20140155 (2015).

²G. G. Howes, “The fundamental parameters of astrophysical plasma turbulence and its dissipation: non-relativistic limit,” *Journal of Plasma Physics* **90**, 905900504 (2024).

³K. G. Klein and G. G. Howes, “Measuring collisionless damping in heliospheric plasmas using field–particle correlations,” *The Astrophysical Journal Letters* **826**, L30 (2016).

⁴G. G. Howes, K. G. Klein, and T. C. Li, “Diagnosing collisionless energy transfer using field–particle correlations: Vlasov–poisson plasmas,” *Journal of Plasma Physics* **83**, 705830102 (2017).

⁵K. G. Klein, G. G. Howes, J. M. TenBarge, and F. Valentini, “Diagnosing collisionless energy transfer using field–particle correlations: Alfvén-ion cyclotron turbulence,” *Journal of Plasma Physics* **86** (2020).

⁶A. Afshari, G. Howes, J. Shuster, K. Klein, D. McGinnis, M. Martinović, S. Boardsen, C. Brown, R. Huang, D. Hartley, *et al.*, “Direct observation of ion cyclotron damping of turbulence in earth’s magnetosheath plasma,” *Nature communications* **15**, 7870 (2024).

⁷K. G. Klein, G. G. Howes, and J. M. TenBarge, “Diagnosing collisionless energy transfer using field–particle correlations: gyrokinetic turbulence,” *Journal of Plasma Physics* **83** (2017).

⁸G. G. Howes, A. J. McCubbin, and K. G. Klein, “Spatially localized particle energization by Landau damping in current sheets produced by strong Alfvén wave collisions,” *J. Plasma Phys.* **84**, 905840105 (2018), arXiv:1708.00757 [physics.plasm-ph].

⁹T. C. Li, G. G. Howes, K. G. Klein, Y.-H. Liu, and J. M. TenBarge, “Collisionless energy transfer in kinetic turbulence: field–particle correlations in fourier space,” *J. Plasma Phys.* **85**, 905850406 (2019).

¹⁰S. A. Horvath, G. G. Howes, and A. J. McCubbin, “Electron landau damping of kinetic alfvén waves in simulated magnetosheath turbulence,” **27**, 102901 (2020).

¹¹C. Chen, K. Klein, and G. G. Howes, “Evidence for electron landau damping in space plasma turbulence,” *Nature communications* **10**, 740 (2019).

¹²A. Afshari, G. Howes, C. Kletzing, D. Hartley, and S. Boardsen, “The importance of electron landau damping for the dissipation of turbulent energy in terrestrial magnetosheath plasma,” *Journal of Geophysical Research: Space Physics* **126**, e2021JA029578 (2021).

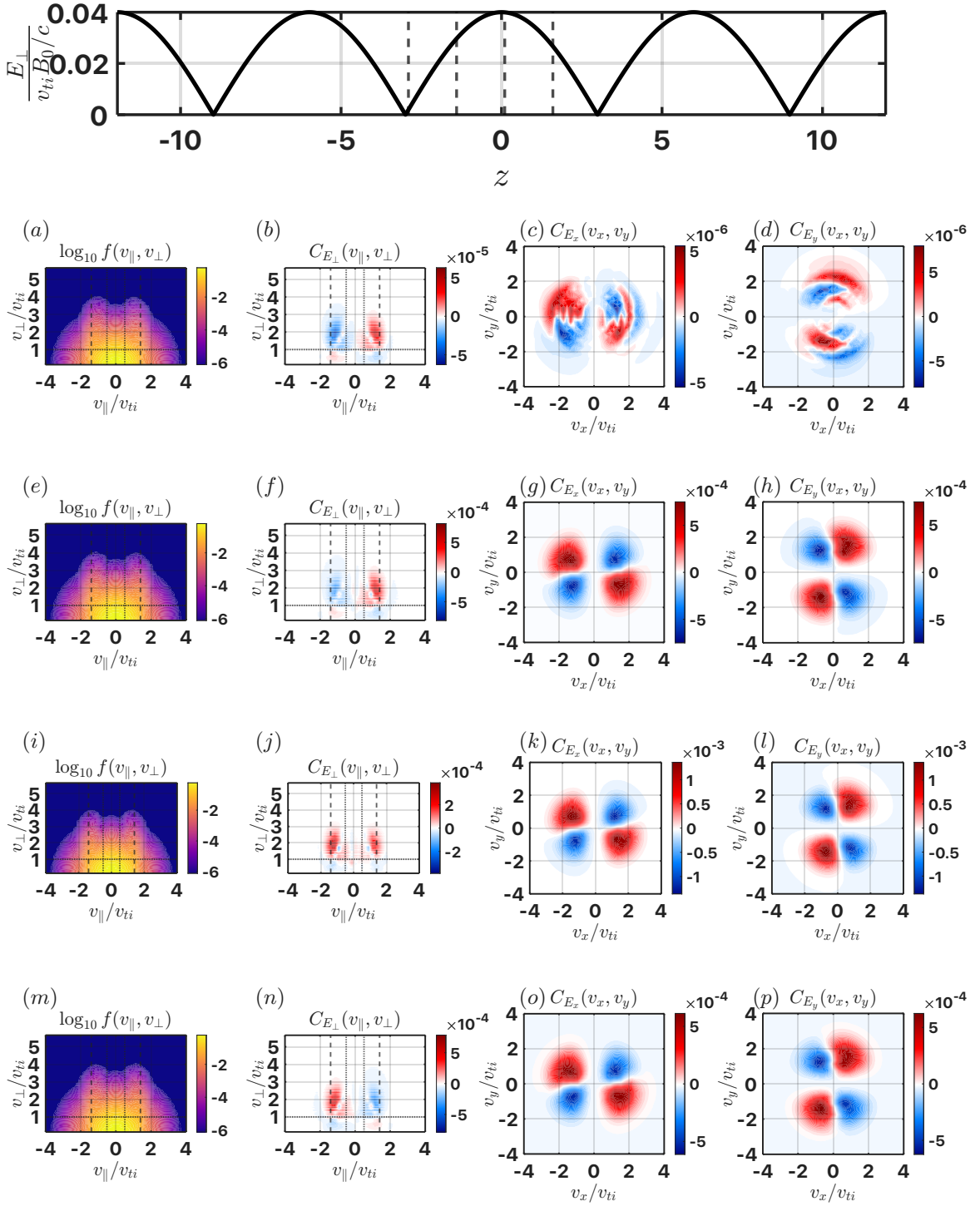


FIG. 13. Asymmetrical velocity-space signatures of ion cyclotron damping in a standing wave pattern due to two counter-propagating ICWs, where the FPC analysis (in the same format as Fig. 6) has been performed at $z/\rho_i = -2.9$ (second row), -1.4 (third row), 0.1 (fourth row), and 1.6 (fifth row).

- ¹³S. A. Conley, G. G. Howes, and A. J. McCubbin, “Characterizing the velocity-space signature of electron landau damping,” *Journal of plasma physics* **89**, 905890514 (2023).
- ¹⁴R. Huang, G. G. Howes, and A. J. McCubbin, “The velocity-space signature of transit-time damping,” *Journal of Plasma Physics* **90**, 535900401 (2024).
- ¹⁵P. Montag and G. G. Howes, “A field-particle correlation analysis of magnetic pumping,” *Physics of plasmas* **29** (2022).
- ¹⁶A. J. McCubbin, G. G. Howes, and J. M. TenBarge, “Characterizing velocity-space signatures of electron energization in large-guide-field collisionless magnetic reconnection,” *Physics of Plasmas* **29**, 052105 (2022).
- ¹⁷J. Juno, G. G. Howes, J. M. TenBarge, L. B. Wilson III, A. Spitkovsky, D. Caprioli, K. G. Klein, and A. Hakim, “A field-particle correlation analysis of a perpendicular magnetized collisionless shock,” *Journal of plasma physics* **87**, 905870316 (2021).
- ¹⁸J. Juno, C. R. Brown, G. G. Howes, C. C. Haggerty, J. M. TenBarge, I. Wilson, Lynn B., D. Caprioli, and K. G. Klein, “Phase-space Energization of Ions in Oblique Shocks,” *Astrophys. J.* **944**, 15 (2023), arXiv:2211.15340 [physics.plasm-ph].
- ¹⁹C. Brown, J. Juno, G. Howes, C. Haggerty, and S. Constantinou, “Isolation and phase-space energization analysis of the instabilities in collisionless shocks,” *J. Plasma Phys.* **89**, 905890308 (2023), arXiv:2211.15786.
- ²⁰G. G. Howes, A. Felix, C. R. Brown, C. C. Haggerty, J. Juno, J. M. TenBarge, L. B. Wilson, and D. Caprioli, “Velocity-space signatures of shock-drift acceleration at quasi-perpendicular collisionless shocks,” *Physics of Plasmas* **32**, 062904 (2025).
- ²¹J. W. Schroeder, G. Howes, C. Kletzing, F. Skiff, T. Carter, S. Vincena, and S. Dorfman, “Laboratory measurements of the physics of auroral electron acceleration by alfvén waves,” *Nature communications* **12**, 3103 (2021).
- ²²P. Montag, G. G. Howes, D. McGinnis, A. S. Afshari, M. J. Starkey, and M. I. Desai, “MMS Observations of the Velocity-space Signature of Shock-drift Acceleration,” **980**, L23 (2025), arXiv:2306.09061 [physics.space-ph].
- ²³S. J. Schwartz, P. W. Daly, and A. N. Fazakerley, “7-multi-spacecraft analysis of plasma kinetics,” in *Analysis Methods for Multi-Spacecraft Data* (ESA Publ. Div., 1998) pp. 159–183.
- ²⁴T. H. Stix, *Waves in plasmas* (Springer Science & Business Media, 1992).
- ²⁵D. Verscharen and B. D. Chandran, “The dispersion relations and instability thresholds of oblique plasma modes in the presence of an ion beam,” *The Astrophysical Journal* **764**, 88 (2013).
- ²⁶R. Huang and G. G. Howes, “The explicit connection between field-particle correlation and distribution function evolution in landau damping,” *Physics of plasmas* (in preparation) (2025).
- ²⁷K. G. Klein and G. G. Howes, “Predicted impacts of proton temperature anisotropy on solar wind turbulence,” *Physics of Plasmas* **22**, 032903 (2015).
- ²⁸K. G. Klein, G. G. Howes, and C. R. Brown, “PLUME: Plasma in a linear uniform magnetized environment,” *Research Notes of the AAS* **9**, 102 (2025).
- ²⁹From this point forward, we omit the species subscript “s” for both the FPCs and the distribution function, as we focus exclusively on ions.
- ³⁰G. G. Howes, “A prospectus on kinetic heliophysics,” **24**, 055907 (2017).
- ³¹J. Squire, R. Meyrand, M. W. Kunz, L. Arzamasskiy, A. A. Schekochihin, and E. Quataert, “High-frequency heating of the solar wind triggered by low-frequency turbulence,” *Nature Astronomy* **6**, 715–723 (2022).
- ³²R. Huang, “Code and Data for: Unveiling the Velocity-Space Signature of Ion Cyclotron Damping Using Liouville Mapping,” (2025).
- ³³W. Jiang, D. Verscharen, S.-Y. Jeong, H. Li, K. G. Klein, C. J. Owen, and C. Wang, “Velocity-space signatures of resonant energy transfer between whistler waves and electrons in the earth’s magnetosheath,” *The Astrophysical Journal* **960**, 30 (2023).
- ³⁴K. Klein, G. Howes, J. TenBarge, S. Bale, C. Chen, and C. Salem, “Using synthetic spacecraft data to interpret compressible fluctuations in solar wind turbulence,” *The Astrophysical Journal* **755**, 159 (2012).
- ³⁵C. Kletzing, “Electron acceleration by kinetic alfvén waves,” *Journal of Geophysical Research: Space Physics* **99**, 11095–11103 (1994).
- ³⁶C. Kletzing and S. Hu, “Alfvén wave generated electron time dispersion,” *Geophysical research letters* **28**, 693–696 (2001).